

IMMUNOLOGY

DExD/H-box helicase 9 intrinsically controls CD8⁺ T cell–mediated antiviral response through noncanonical mechanisms

Anjun Jiao^{1,2,3,4†}, Chenming Sun^{1,2,4†}, Xin Wang^{1,2,4†}, Lei Lei^{1,2,4†}, Haiyan Liu^{1,2†}, Wenhui Li^{5,6}, Xiaofeng Yang^{1,2,4}, Huiqiang Zheng^{1,2}, Renyi Ding^{1,2}, Kun Zhu^{1,2}, Yanhong Su^{1,2}, Cangang Zhang^{1,2}, Lianjun Zhang^{5,6*}, Baojun Zhang^{1,2,3,4*}

Upon virus infection, CD8⁺ T cell accumulation is tightly controlled by simultaneous proliferation and apoptosis. However, it remains unclear how TCR signal coordinates these events to achieve expansion and effector cell differentiation. We found that T cell–specific deletion of nuclear helicase Dhx9 led to impaired CD8⁺ T cell survival, effector differentiation, and viral clearance. Mechanistically, Dhx9 acts as the key regulator to ensure LCK- and CD3ε-mediated ZAP70 phosphorylation and ERK activation to protect CD8⁺ T cells from apoptosis before proliferative burst. Dhx9 directly regulates *Id2* transcription to control effector CD8⁺ T cell differentiation. The DSRM and OB_Fold domains are required for LCK binding and *Id2* transcription, respectively. Dhx9 expression is predominantly increased in effector CD8⁺ T cells of COVID-19 patients. Therefore, we revealed a previously unknown regulatory mechanism that Dhx9 protects activated CD8⁺ T cells from apoptosis and ensures effector differentiation to promote antiviral immunity independent of nuclear sensor function.

INTRODUCTION

Upon viral infection, naïve CD8⁺ T cells are activated by cognate antigens and differentiate into either short-lived effector T cells or memory precursor effector T cells, which further differentiate into memory lineage and mediate long-term protective immunity (1–7). The efficacy of viral clearance is highly dependent on clonal expansion, acquisition of effector functions, and survival of effector CD8⁺ T cells. In the last two decades, it has been demonstrated that T cell receptor (TCR) signaling, transcriptional factors, and cytokines are coordinated to regulate multiple key events of this process (1, 2, 8–10). TCR signaling initiates CD8⁺ T cell activation, and both TCR signal strength and duration play key roles to control expansion and functional differentiation (2, 11–13). Following initial TCR activation, CD8⁺ T cell proliferation, differentiation, and survival are controlled by multiple pairs of transcription factors such as *Id2* (2, 14), *T-bet* (15), *Blimp-1* (15–19), *IRF4* (20), and *BATF* (21). Yet, it remains largely unknown how TCR signal is integrated and transduced to control CD8⁺ T cell fate decision.

Innate pattern recognition receptors predominantly trigger innate immune response by recruiting adaptor proteins such as MyD88 and TRIF [Toll-interleukin receptor (TIR) domain–containing adapter-inducing interferon-β (IFN-β)], which subsequently activate downstream signaling of nuclear factor κB (NF-κB) and IFN regulatory factor (IRF) to produce IFN I and other proinflammatory cytokines (22–25). Dhx9, a cytosolic nuclear sensor recognizing viral DNA or

RNA (26, 27), also known as RNA helicase A (RHA), is capable of unwinding genomic RNA and DNA (28, 29). It consists of a conserved helicase core domain, two double-stranded RNA binding domains, a nuclear transport domain, and a single-stranded DNA binding RGG box domain (30). As a nuclear sensor, Dhx9 plays critical roles in innate immune cell–mediated response against viral infection. Dhx9, which recognizes CpG-B from viral DNA via the DUF1605 domain, can bind to the TIR domain of MyD88 and activate NF-κB and IRF7 in plasmacytoid dendritic cells (DCs) to produce tumor necrosis factor α (TNFα) and interleukin-6 (IL-6) (26). Dhx9 can also bind to polyinosinic-polycytidylic acid or interact with IPS-1 via the helicC-HA2-DUF domain to activate NF-κB and IRF3 in myeloid DCs, leading to the production of IFN-α/β and other proinflammatory cytokines (27).

In addition to DNA sensing, Dhx9 uses its adenosine triphosphatase (ATPase)/helicase activity to recruit RNA polymerase II (RNAPII) to the corresponding promoters to enhance inflammatory cytokine production in macrophages (31). This process does not involve the induction of the cytoplasmic translocation of Dhx9, which requires the ATPase-dependent helicase (ATPase/helicase) domain but not the cytosolic DNA sensing domain. Dhx9 is also reported to assist Nlrp9b in recognizing short double-stranded RNA to form inflammasome complexes and induce gasdermin D–induced pyroptosis (32). This raises the possibility that Dhx9 may execute key regulatory roles independent of nuclear sensor activity. Moreover, recent findings demonstrated that T cells also use innate signaling pathways to initiate antiviral response (33–35), such as stimulation of cytokine production (36) and delivery of costimulatory signals (37). With transposon-induced Dhx9 deficiency mouse model, one previous study demonstrated that Dhx9 is also required for T cell development in both the thymus and periphery (38). However, it is unknown whether Dhx9 is directly involved in the regulation of CD8⁺ T cell fate decision during antiviral response.

To this end, we characterized the role of nuclear sensor Dhx9 in the regulation of CD8⁺ T cell proliferation, survival, effector

Copyright © 2022 The Authors, some rights reserved; exclusive licensee American Association for the Advancement of Science. No claim to original U.S. Government Works. Distributed under a Creative Commons Attribution NonCommercial License 4.0 (CC BY-NC).

¹Department of Pathogenic Microbiology and Immunology, School of Basic Medical Sciences, Xi'an Jiaotong University, Xi'an, Shaanxi, China. ²Institute of Infection and Immunity, Translational Medicine Institute, Xi'an Jiaotong University Health Science Center, Xi'an, Shaanxi, China. ³Key Laboratory of Environment and Genes Related to Diseases, Xi'an Jiaotong University, Xi'an, Shaanxi, China. ⁴Xi'an Key Laboratory of Immune Related Diseases, Xi'an, Shaanxi, China. ⁵Institute of Systems Medicine, Chinese Academy of Medical Sciences and Peking Union Medical College, Beijing 100005, China. ⁶Suzhou Institute of Systems Medicine, Suzhou 215123, China.

*Corresponding author. Email: bj.zhang@mail.xjtu.edu.cn (B.Z.); zlj@ism.cams.cn (L.Z.)

†These authors contributed equally to this work.

differentiation, and function during viral/bacterial infection. Our data showed that specific deletion of Dhx9 in T cells caused an impaired viral clearance and lower animal survival rate against infection, with severe defects in the accumulation of antigen-specific CD8⁺ T cells. Unexpectedly, loss of Dhx9 led to unusual apoptosis at the early stage of T cell activation. Mechanistically, Dhx9 ensures CD8⁺ T cell survival even before proliferation and effector differentiation as a key component of the CD3ε-LCK-ZAP70 complex to allow LCK-mediated ZAP70 phosphorylation, and Dhx9 further controls Bim and Bcl-2 expression by modulating extracellular signal-regulated kinase (ERK) phosphorylation. Using multiomics analysis combined with retrovirus-based gene manipulation, we also provide evidences that Dhx9 controls effector CD8⁺ T cell differentiation by directly binding and regulating *Id2* gene expression while indirectly regulating several key genes required for effector differentiation. The DSRM and OB_Fold domains of Dhx9 are required to regulate LCK-mediated ZAP70 phosphorylation and *Id2* transcription, respectively. Therefore, we provide compelling evidences that Dhx9 is required for a productive CD8⁺ T cell response against viral infection by directly orchestrating TCR signal transduction to protect T cells from cell death upon early activation and regulating genes critical for effector T cell differentiation via nuclear sensor-independent manner.

RESULTS

Loss of Dhx9 impairs the accumulation of CD8⁺ effector and memory T cells upon viral infection

Since Dhx9 is involved in innate cell-mediated antiviral immunity, we aim to investigate whether Dhx9 mediates antiviral response by directly regulating CD8⁺ T cell differentiation and functionality. To this end, we generated T cell-specific Dhx9 knockout mice (Dhx9^{TKO}) by crossing Dhx9 flox mice (fig. S1A) with CD4-Cre transgenic strain (fig. S1, B and C). There were no developmental abnormalities for CD4⁺ and CD8⁺ T cells in the thymi and spleens after Dhx9 deletion (fig. S2, A to C). To further investigate the role of Dhx9 in CD8⁺ T cell immunity to viral infection, we infected wild-type (WT) and Dhx9^{TKO} mice with 2×10^5 colony-forming units (CFU) lymphocytic choriomeningitis virus (LCMV) Armstrong or rechallenged the mice with *Listeria monocytogenes* (LM) expressing GP33. We found that Dhx9^{TKO} mice showed a decreased survival rate during both primary infection (Fig. 1A, top panel) and antigen rechallenge (Fig. 1A, bottom panel). Increased severity of virus infection was also observed in Dhx9^{TKO} mice, as a higher viral load in the liver tissues from Dhx9^{TKO} mice was confirmed by quantitative polymerase chain reaction (qPCR) (Fig. 1B). In addition, the size of the spleen, the absolute cell number of total splenocytes, and CD8⁺ T cells from Dhx9^{TKO} mice were markedly reduced compared to WT counterparts (Fig. 1C). Given the significance of CD8⁺ T cells in antiviral response, we thus analyzed the percentages and absolute numbers of antigen-specific CD8⁺ T cells in response to LCMV infection. Our data showed that Dhx9 deletion caused a marked reduction in both percentages and absolute numbers of splenic CD8⁺GP33⁺ cells on both day 5 (Fig. 1, D, E, and G) and day 8 (Fig. 1, D, F, and H) after infection. To further confirm whether the reduced CD8⁺ T cell response is CD8⁺ T cell intrinsic, we cotransferred either WT or Dhx9^{-/-} naïve CD8⁺ T cells at a 2:3 ratio, together with WT naïve CD4⁺ T cells. Similar results were recapitulated 4 days (Fig. 1, I and J, and fig. S3, A and B) and 8 days (Fig. 1, I and K, and fig. S3, A and

B) after LCMV infection. Accordingly, on day 90 after infection, the percentage and number of CD8⁺GP33⁺ T cells in the memory phase markedly decreased in Dhx9^{TKO} mice compared to WT mice (Fig. 1, L and M), resulting in an impaired recall response upon rechallenge with LM-GP33 (Fig. 1, L and N). To further consolidate this phenotype, we used a transgenic TCR model by cotransferring WT (CD45.1) and Dhx9^{-/-} (CD45.2) OT-1 CD8⁺ T cells at the ratio of 1:1 into the same recipient mice (CD45.1 and CD45.2), which was followed by infection with LM-ovalbumin (OVA). Consistently, Dhx9^{-/-} CD8⁺ OT-1 T cells displayed similar accumulation defects as in LCMV infection model (fig. S3, C and D). Together, these observations support that Dhx9 acts as a critical intrinsic factor to control CD8⁺ T cell effector cell accumulation and adaptive immunity in response to viral/bacterial infection.

Dhx9 is required for the survival of activated CD8⁺ T cells by regulating Bcl-2/Bim expression

Next, we sought to determine whether the decreased antigen-specific CD8⁺ T cell accumulation during infection was caused by reduced proliferation or increased cell death. Both 5-bromo-2'-deoxyuridine (BrdU) incorporation (fig. S4, A and B) and Ki67 (fig. S4, C and D) staining suggested a slight decrease of proliferating cells in Dhx9^{-/-} groups 48 hours after stimulation *in vitro*. However, we observed a reduction of BrdU incorporation and Ki67 expression in Dhx9^{-/-} cells at early time point upon LCMV infection (fig. S4, E, F, H, and I) and LM-OVA infection (fig. S4, K and L), whereas a slight increase of BrdU incorporation and Ki67 expression was shown in Dhx9^{-/-} cells at later time point upon LCMV infection (fig. S4, E, G, H, and J) and LM-OVA infection (fig. S4, M and N). Of note, we observed a significantly higher percentage of Dhx9^{-/-} CD8⁺GP33⁺ T cells undergoing apoptosis compared to WT counterparts on both day 5 (Fig. 2, A and B) and day 8 (Fig. 2, A and C) after infection. In the cotransfer model, a significantly higher percentage of apoptotic cells (annexin V⁺7AAD⁺ and annexin V⁺7AAD⁻) was also observed in Dhx9^{-/-} CD8⁺GP33⁺ T cells and Dhx9^{-/-} CD8⁺OT-1⁺ cells as compared to WT T cells on day 4 (fig. S5, A, C, and D) and day 8 (fig. S5, B, C, and E) after infection. Furthermore, the apoptotic phenotype was confirmed at 48 hours (Fig. 2, D and E) following stimulation with anti-CD3/CD28 antibodies (Abs) *in vitro*. However, we observed similar frequency of apoptotic cells when WT or Dhx9^{-/-} CD8⁺ T cells were cultured with IL-7 (Fig. 2, D and F).

To further confirm that Dhx9 deletion led to increased apoptosis of activated CD8⁺ T cells, we measured the expression pattern of classic pro- and anti-apoptotic proteins. In comparison to WT counterparts, Dhx9^{-/-} CD8⁺ T cells showed notably increased caspase 3 and Bim expression, whereas the Bcl-2 expression was markedly decreased at 24 and 48 hours following *in vitro* stimulation (Fig. 2G). Treatment with inhibitors of caspase 8, caspase 9, or pan-caspase was able to improve both viability and absolute cell number of Dhx9^{-/-} cells to the level similar to WT T cells (fig. S6, A to C), confirming the role of Dhx9 in supporting survival of activated CD8⁺ T cells. Moreover, Bcl-2 overexpression in Dhx9-deficient CD8⁺ T cells was able to rescue cell death both *in vitro* (Fig. 2, H and I) and *in vivo* (Fig. 2, J and K). Bcl-2 overexpression could rescue the percentage and absolute number of Dhx9-deficient CD8⁺ T cells to the WT level (Fig. 2, L to N).

Of note, we found more apoptotic (annexin V⁺) cells in non-divided cells of Dhx9^{-/-} group compared to WT group (fig. S4O). Although there was comparable level of dividing cells in each

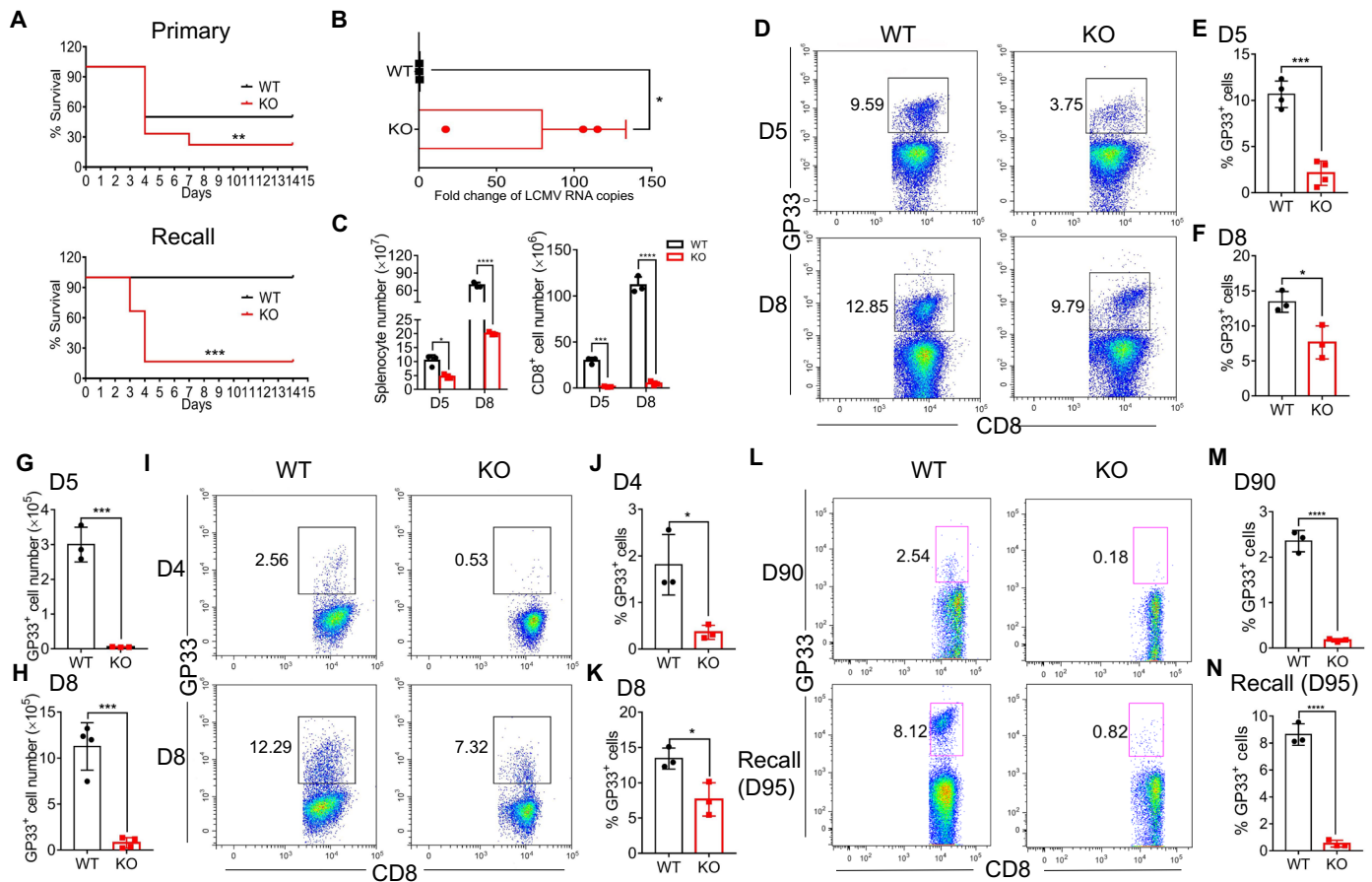


Fig. 1. Impaired accumulation of CD8⁺ T cells in Dhx9^{TKO} mice upon infection. (A) Survival curves for primary LM-GP33 infection (2×10^5 CFU per mouse; $n = 8$ mice per group; top) and recall response ($n = 8$ mice per group; bottom). For recall experiment, WT or KO mice were infected with 2×10^5 PFU of LCMV and then rechallenged with 5×10^5 CFU LM-GP33 90 days later. (B) Wild-type (WT) and Dhx9^{TKO} (KO) mice were immunized with 2×10^5 CFU LCMV-Armstrong. The liver mRNA levels of LCMV from WT and KO mice were analyzed 8 days after LCMV infection by qPCR; the fold change was normalized to WT group; ($n = 3$ mice per group). (C to H) WT and CD4Cre⁺Dhx9^{fl/fl} (KO) mice were challenged with 2×10^5 PFU of LCMV by intraperitoneal injection. Cell numbers of splenocytes and CD8⁺ T cells were examined 5 and 8 days after LCMV infection (C). GP33-specific CD8⁺ T cells in both mice were measured by flow cytometry. Representative FACS plots of GP33-specific CD8⁺ T cells (D); percentage (E and F) and number of GP33⁺CD8⁺ T cells (G and H) ($n = 3$ to 4 mice per group). (I to K) WT and KO naive CD8⁺ T cells at a ratio of 2:3 together with naive WT CD4⁺ T cells were cotransferred into recipient mice (4.5-Gy irradiation) followed by challenge with 2×10^5 PFU of LCMV. Four and eight days later, donor GP33-specific CD8⁺ T cells were measured by flow cytometry. Representative FACS plots (I) and the percentage of GP33-specific CD8⁺ T cells (J and K) ($n = 3$ mice per group). (L to N) LCMV-infected WT or KO mice (90 days) or mice reinfected with 5×10^5 CFU LM-GP33 by intravenous injection for 4 days. GP33-specific CD8⁺ T cells from indicated mice were analyzed by FACS. Representative FACS plots (L) and the percentage of GP33-specific CD8⁺ T cells (M and N) ($n = 3$ mice per group). Data are representative of at least three independent experiments shown as the means \pm SEM. Statistical testing is depicted as two-sided, unpaired *t* tests; * $P \leq 0.05$; ** $P \leq 0.01$; *** $P \leq 0.001$; **** $P \leq 0.0001$.

generation of live cells (annexin V⁻) between two groups (fig. S4P), Dhx9^{-/-} cells showed higher percentages of dead cells (annexin V⁺) in undivided and first dividing generation (fig. S4Q). Together, our results suggest that increased apoptosis rather than proliferation defects is the major cause for the decreased accumulation of Dhx9^{-/-} CD8⁺ T cells upon viral infection and TCR stimulation.

ERK is required for Dhx9-controlled Bcl-2 expression and CD8⁺ T cell survival

Next, we sought to determine which signaling pathway downstream of TCR is involved in regulating CD8⁺ T cell survival. WT and Dhx9^{-/-} CD8⁺ T cells were thus stimulated with anti-CD3 and anti-CD28 Abs in the presence of p38, ERK, or c-Jun N-terminal kinase (JNK) inhibitors or agonists for 48 hours. We found that inhibition of ERK or JNK led to an increased apoptosis of WT cells (Fig. 3, A and C). In contrast,

ERK, but not JNK, agonist rescued cell death of Dhx9^{-/-} cells (Fig. 3, B and D). Consistently, ERK inhibitor could suppress Bcl-2 expression and increase Bim expression in both activated WT and Dhx9-deficient CD8⁺ T cells, while ERK agonist was able to increase Bcl-2 but reduce Bim expression in Dhx9-deficient CD8⁺ T cells (Fig. 3G). We found that addition of ERK inhibitor at the beginning of TCR stimulation significantly increased apoptosis of activated CD8⁺ T cells, whereas administration of ERK inhibitor 6 or 12 hours after TCR stimulation did not affect cell survival (Fig. 3, E and F), indicating that early ERK activation is an essential survival signal for activated T cells. We found impaired activation of ERK signaling in Dhx9-deficient CD8⁺ T cells upon stimulation with anti-CD3 plus anti-CD28 Abs for 5 to 10 min (Fig. 3H). Collectively, those findings suggest that Dhx9 is required for proper ERK activation to balance Bim and Bcl-2 expression and support the survival of activated CD8⁺ T cells.

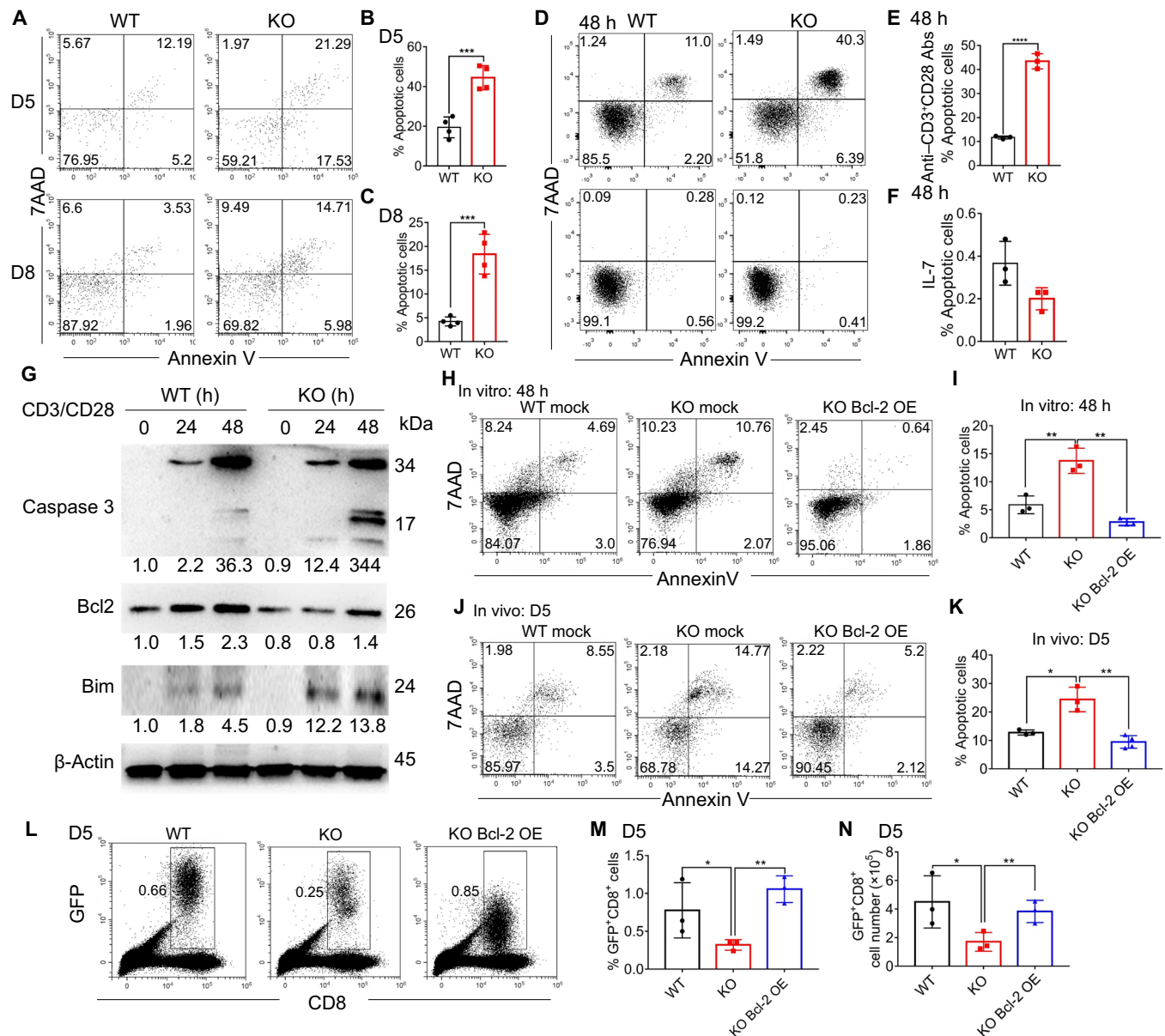


Fig. 2. Loss of Dhx9 led to increased apoptosis of CD8⁺ T cells through declining Bcl-2 expression. (A) Representative FACS plots of annexin V and 7AAD expression in GP33⁺CD8⁺ T cells from WT and KO mice infected with 2×10^5 PFU of LCMV. (B and C) Percentage of apoptotic cells 5 and 8 days after infection ($n = 4$ mice per group). (D) Representative FACS plots of annexin V and 7AAD expression in WT and KO CD8⁺ T cells stimulated with anti-CD3 (5 μ g/ml)/anti-CD28 (2 μ g/ml) Abs or IL-7 (5 ng/ml) for 48 hours. (E) Percentage of apoptotic cells with anti-CD3 and anti-CD28 Ab stimulation. (F) Percentage of apoptotic cells with IL-7 culture ($n = 3$ wells per group). (G) WT and KO naïve CD8⁺ T cells were stimulated with anti-CD3 (5 μ g/ml) and anti-CD28 (2 μ g/ml) Abs for 24 and 48 hours. The protein levels of Bcl-2, Bim, and caspase 3 were measured by Western blot and quantified by normalizing to β -actin. (H and I) Representative FACS plots and percentage of annexin V and 7AAD expression in in vitro stimulated CD8⁺ T cells from indicated groups ($n = 3$ wells per group). (J to N) WT and KO OT-1⁺CD8⁺ T cells were stimulated with concanavalin A (2 μ g/ml) for 12 hours in vitro and then infected with either mock or Bcl-2-overexpressing (OE) retrovirus for 24 hours. GFP⁺CD8⁺CD62L⁺CD44⁻ cells were sorted and adoptively transferred into WT mice followed by infection with 2×10^5 CFU LM-OVA. (J and K) Representative FACS plots and percentage of annexin V and 7AAD expression in CD8⁺ T cells after 5 days of infection from indicated groups. (L) Representative FACS plots of CD8 and GFP expression in the spleens. Percentage (M) and absolute number of GFP⁺CD8⁺ T cells in spleens (N) ($n = 3$ mice per group). Data are representative of at least three independent experiments shown as the means \pm SEM. Statistical testing is depicted as two-sided, unpaired t tests; * $P \leq 0.05$; ** $P \leq 0.01$; *** $P \leq 0.001$.

Dhx9 interacts with CD3 ϵ -LCK-ZAP70 to facilitate ZAP70 phosphorylation

To determine how Dhx9 regulates TCR-induced ERK activation, we first assessed several well-known targets controlled by Dhx9 in innate cells. However, Dhx9 deficiency did not alter the activity of

p65, p100, and IRF7 after TCR stimulation (fig. S7A). Next, we performed mass spectrometry (MS) with activated WT CD8⁺ T cells to investigate the potential binding partners that may affect ERK activation (fig. S8). Among 163 proteins obtained using pull-down assay with Dhx9 Ab (table S1), 48 candidate proteins were selected

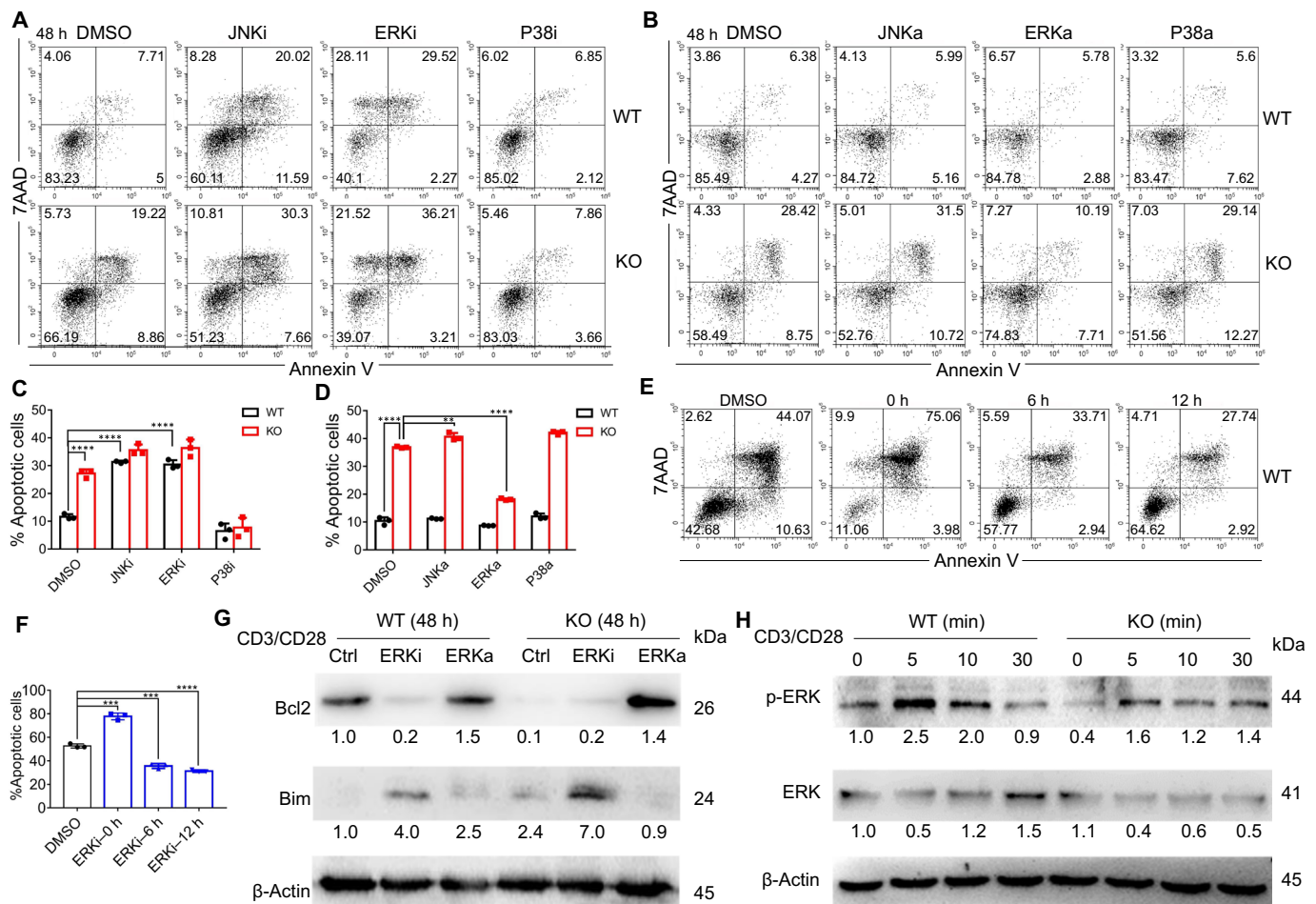


Fig. 3. Impaired ERK activation is responsible for decreased Bcl-2 expression and increased apoptosis. (A) WT and KO naïve CD8⁺ T cells were pretreated with inhibitors of JNK (5 μM), ERK (20 μM), or p38 (25 μM) for 30 min, followed by treatment with anti-CD3 (5 μg/ml) and anti-CD28 (2 μg/ml) Abs for 48 hours. The expression of annexin V and 7AAD in CD8⁺ T cells with indicated treatments. DMSO, dimethyl sulfoxide. (B) WT and KO naïve CD8⁺ T cells were stimulated with agonists of JNK (100 nM), ERK (50 μM), or p38 (5 μM) in the presence of anti-CD3 and anti-CD28 Abs for 48 hours. Representative FACS plots of annexin V and 7AAD staining in CD8⁺ T cells with indicated treatments. (C and D) Percentage of apoptotic CD8⁺ T cells in (A) and (B), respectively (*n* = 3 well per group). (E) WT naïve CD8⁺ T cells were stimulated with anti-CD3 (5 μg/ml) and anti-CD28 (2 μg/ml) Abs, with addition of ERK inhibitor (20 μM) at 0, 6, and 12 hours. The expression of annexin V and 7AAD in CD8⁺ T cells was assessed at 48 hours. (F) Percentage of apoptotic CD8⁺ T cells in (E). (G) Expression of Bcl-2 and Bim in stimulated WT and KO CD8⁺ T cells. WT and KO naïve CD8⁺ T cells were pretreated with ERK inhibitor or ERK agonist for 30 min, followed by treatment with anti-CD3 and anti-CD28 Abs for 48 hours. The protein levels of Bcl-2 and Bim were measured by Western blot. The protein levels were quantified and normalized to β-actin. (H) ERK activation in stimulated WT and KO CD8⁺ T cells. Naïve CD8⁺ T cells from WT and KO mice were stimulated with anti-CD3 and anti-CD28 Abs for 0, 5, 10, and 30 min. The levels of indicated proteins were measured by Western blot. The protein levels were quantified and normalized to β-actin. Data are representative of at least three independent experiments shown as the means ± SEM. Statistical testing is depicted as two-sided, unpaired *t* tests; **P* < 0.05; ***P* < 0.01; ****P* < 0.001; *****P* < 0.0001.

(Fig. 4A) after excluding housekeeping proteins such as ribosomal proteins, actin, and tubulin. LCK was considered as a top candidate given its important role in TCR signaling network. Dhx9^{-/-} T cells showed a reduced phosphorylation of ZAP70 as well as reduced expression of Egr1, but not Egr2/3 (fig. S7B), in response to TCR stimulation, although LCK expression was comparable between WT and Dhx9^{-/-} T cells (Fig. 4B). In addition, we found that Dhx9 is bound to CD3ε, LCK, and ZAP70 in unstimulated CD8⁺ T cells. Notably, the binding of Dhx9 to ZAP70 upon TCR stimulation was weaker, although it remained bound to LCK and CD3ε (Fig. 4C). This was further validated through immunoprecipitation with anti-ZAP70 Abs (Fig. 4D). The binding of LCK to CD3ε and ZAP70 was dramatically reduced in stimulated Dhx9^{-/-} T cells in comparison to that in WT control (Fig. 4E). To demonstrate which

domain of Dhx9 is required for LCK binding, we thus transduced vectors overexpressing distinct domains as indicated together with hemagglutinin (HA) tag in 293T cells (Fig. 4F). Both full-length Dhx9 and #1 vector (with only RGG domain missing) could efficiently bind to LCK, which indicated that RGG domain is not required for Dhx9 binding to LCK (Fig. 4G). Comparing to #1, #6 vector had DSRM domain mutated and lost its binding to LCK, which demonstrated that the binding of Dhx9 to LCK is dependent on the DSRM domain (Fig. 4, G and H, and fig. S9). In summary, our findings suggest that Dhx9 is essential for the phosphorylation of ZAP70 by LCK and CD3ε to transduce TCR downstream signals.

We further investigate the function of DSRM domain in T cell survival by overexpressing #1 or #6 vector in Dhx9-deficient CD8⁺ T cells under TCR stimulation. Our data showed that overexpression

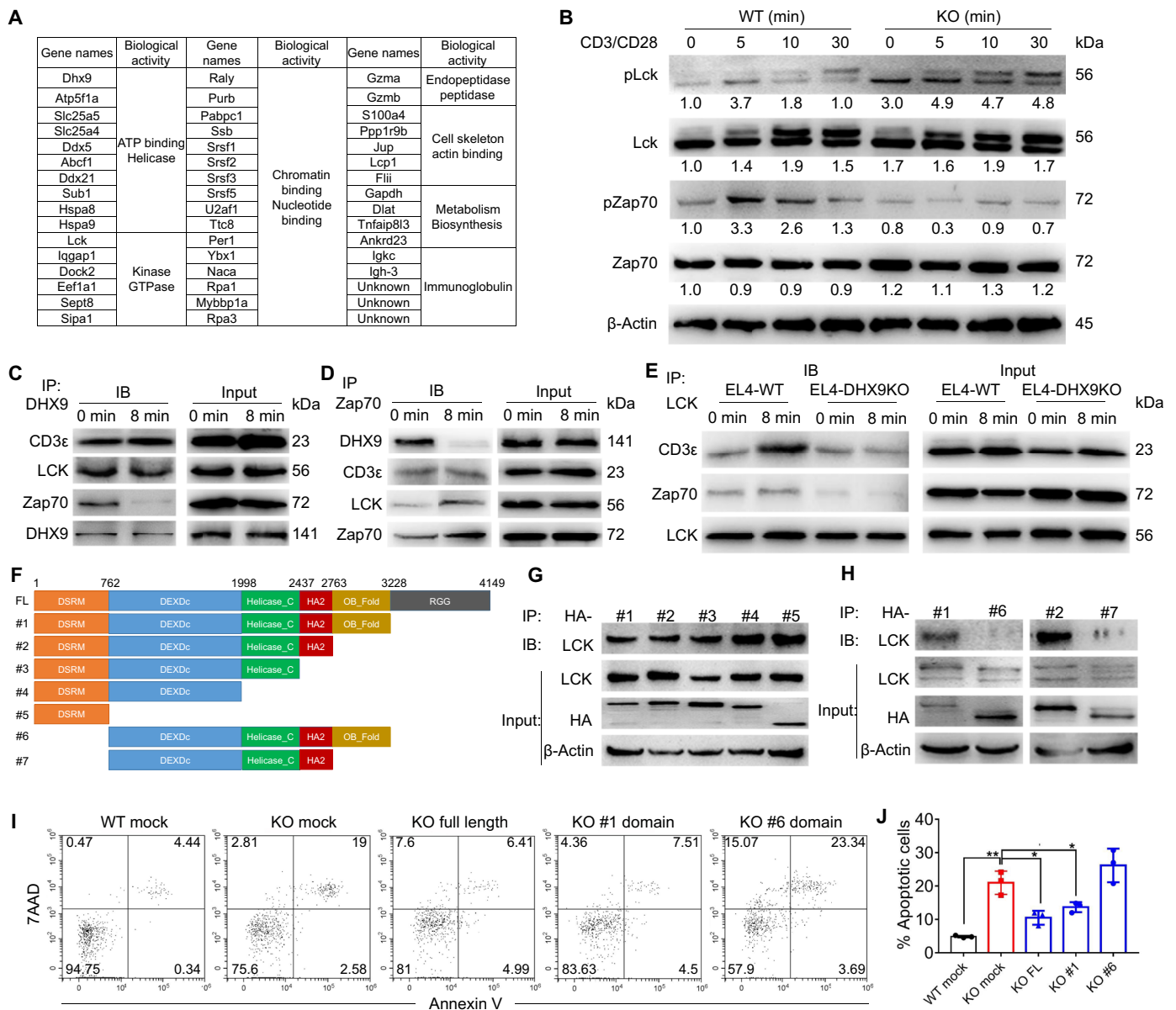


Fig. 4. Dhx9 functions as a component of the complex involving CD3ε, LCK, and ZAP70 to induce ZAP70 phosphorylation. (A) Gene list of Dhx9-binding proteins classified into groups by biological functions. (B) Protein expression of LCK and ZAP70 in naïve CD8⁺ T cells from WT and KO mice stimulated with anti-CD3 and anti-CD28 Abs for 0, 5, 10, and 30 min. Protein levels were measured by Western blot and quantified by normalizing to β-actin. (C) Immunoprecipitation (IP) of CD3ε, LCK, and ZAP70 from stimulated CD8⁺ T cells by Ab against Dhx9, followed by immunoblotting (IB) with CD3ε, LCK, and ZAP70 Abs. (D) IP of Dhx9, CD3ε, and LCK by ZAP70, followed by IB with Dhx9, CD3ε, and LCK Abs. (E) IP of CD3ε and ZAP70 by LCK, followed by IB with CD3ε and ZAP70 Abs. (F to H) HA-tagged distinct domains of Dhx9 together with LCK protein were incubated with HA Ab for IP and LCK Ab for immunoblotting. Schematic representation of the domain structure and plasmid constructs of Dhx9 protein as indicated. DSRM, double-stranded RNA-binding motif; DEXDc, DEAD-like helicase superfamily; Helicase_C, helicase conserved C-terminal domain; HA2, helicase-associated domain; OB_Fold, oligonucleotide/oligosaccharide-binding (OB) fold; RGG, G quadruplex-binding domain (F); (G) for #1 to #5 plasmid; (H) for #1, #6, #2, and #7 plasmid. (I and J) WT and KO CD8⁺ T cells were stimulated with anti-CD3 and anti-CD28 Abs for 12 hours and then infected with either mock-GFP-, Dhx9 full-length GFP-, #1 domain-GFP-, or #6 domain-GFP-overexpressing retrovirus for 48 hours. (I) Representative FACS plots of annexin V and 7AAD staining. (J) Percentage of apoptotic CD8⁺ T cells in indicated groups (n = 3 wells per group). Data are representative of at least three independent experiments shown as the means ± SEM. Statistical testing is depicted as two-sided, unpaired t tests; *P ≤ 0.05; **P ≤ 0.01.

of #1 vector, but not #6 vector, rescued the defects of cell death in Dhx9-deficient CD8⁺ T cells, which was similar to overexpression of full-length Dhx9 (Fig. 4, I and J). Therefore, DSRM domain is also functionally required for the survival of activated CD8⁺ T cells.

Dhx9 is required for the CD8⁺ T cell effector differentiation program

Given that Dhx9 critically regulates CD8⁺ T cell effector differentiation in response to viral infection, we thus examined the expression pattern of Dhx9 following in vitro or in vivo TCR stimulation.

We found that the expression of *Dhx9* at both mRNA and protein levels was unchanged within 30 min but markedly increased 24 and 48 hours after stimulation with anti-CD3/CD28 Abs in vitro (Fig. 5A and figs. S10, A and B, and S11A). Similarly, *Dhx9* expression was up-regulated 5 and 8 days following LCMV infection (Fig. 5B and fig. S11B). Using flow cytometry analysis, we further confirmed a basal level of *Dhx9* expression in naïve T cells, whereas the expression was notably increased upon the stimulation with anti-CD3 and anti-CD28 Abs for 48 hours (Fig. 5C) as well as on day 5 after LCMV infection (Fig. 5D). Consistently, *Dhx9* transcription was significantly increased in CD8⁺ T cells 7 days after LM infection (fig. S13). Of note, the increased expression was specific to effector and effector memory populations, but not in contracting (14 days after infection) and central memory populations (42 days after infection) (fig. S13). Using confocal microscopy, we further confirmed the increased expression of *Dhx9* in both the cytoplasm and nuclei of CD8⁺ T cells activated with anti-CD3/CD28 Abs for 48 hours in vitro and mice infected with LCMV for 5 days (Fig. 5E). We noticed that *Dhx9* was primarily expressed in the nucleus of CD8⁺ T cells from mice infected with LCMV for 5 days, indicating that *Dhx9* may play important roles during this time frame. Collectively, the expression pattern of *Dhx9* implicates its potential role in effector T cell differentiation.

We found that the percentages of CD44⁺CD62L⁻ and KLRG1⁺IL-7R⁻ effector populations were significantly decreased in *Dhx9*^{TKO} mice compared with WT mice on day 5 (Fig. 5, F, G, I, and J) and day 8 (Fig. 5, F, H, I, and K) after infection. In the cotransfer model, *Dhx9*-deficient cells showed similar defects in the effector populations on day 4 (Fig. 5, L and N, and fig. S12, A, B, F, G, I, and J) and day 8 (Fig. 5, M to O, and fig. S10, A, B, F, H, I, and K). Consistently, we observed a significant decrease of intracellular IFN γ expression in *Dhx9*^{TKO} mice within individual transfer experiments (fig. S12, C to E and L to N). To elucidate the regulatory mechanism, we performed RNA sequencing (RNA-seq) on WT and *Dhx9*^{-/-} splenic CD8⁺GP33⁺ T cells 8 days after infection. The quality of sample and sequencing was validated in fig. S14 (A and B and C to G). The analysis revealed 1431 up-regulated genes and 673 down-regulated genes in *Dhx9*^{-/-} cells compared to WT cells (fig. S14H and table S2). In the scatter plot, we observed the down-regulation of several genes associated with effector differentiation (*Id2*, *Tbx21*, *KLRG1*, *Klf2*, *Zeb2*, *Idh2*, *Ccr2*, *Ccl5*, etc.) and the up-regulation of two negative regulators for effector function (*Id3* and *Tox2*) (Fig. 5P). Gene set enrichment analysis (GSEA) pathway analysis further showed that the down-regulated genes were enriched in pathways required for activated or effector T cells (Fig. 5Q). The heat map displayed 37 markedly changed genes associated with effector phenotype based on twofold change as a cutoff (Fig. 5R). Therefore, loss of *Dhx9* significantly diminished effector differentiation program in addition to cell survival defects.

Dhx9 controls effector differentiation by directly regulating *Id2* transcription

To determine whether the changes of these differentially expressed genes are mediated through direct binding of *Dhx9* to the regulatory regions or changing the opening status of chromatin, we performed chromatin immunoprecipitation sequencing (ChIP-seq) analysis on WT CD8⁺GP33⁺ T cells and assay for transposase-accessible chromatin with high-throughput sequencing (ATAC-seq) analysis on WT and *Dhx9*^{-/-} CD8⁺GP33⁺ T cells. The quality of ChIP-seq and ATAC-seq data was confirmed in figs. S15 (A to I) and S16 (A to D), respectively. We screened 3581 binding peaks in WT

CD8⁺GP33⁺ cells by ChIP-seq analysis and 13,243 peaks in WT but not *Dhx9*^{-/-} effector cells by ATAC-seq analysis. Following the overlay analysis of genes from different screens (RNA-seq, ChIP-seq, and ATAC-seq), 57 genes were identified as the top potential targets of *Dhx9* gene in effector CD8⁺ T cells (Fig. 6A and tables S3 and S4). According to the expression level [reads per kilobase of exon model per million mapped reads (RPKM)] and fold change, the top 20 genes were further selected (Fig. 6B). The qPCR validation and ChIP-seq data for top 20 candidate genes are listed in supplementary figures (figs. S17, A and B, and S18). Among the top 20 genes, *Id2* was selected as the top candidate due to the following reasons: (i) The transcription level was the highest among the top candidates (Fig. 6B); (ii) the *Id2* locus in WT effector T cells was notably more open than that in WT naïve cells and KO effectors based on ATAC-seq data (Fig. 6C); and (iii) ChIP-seq data showed a sizable peak at the *Id2* promoter region in WT DNA compared with input (Fig. 6C). Moreover, we showed that *Id2* transcription is down-regulated and up-regulated in T cells with *Dhx9* deficiency and overexpression, respectively (Fig. 6, D and E). Overall, these findings strongly suggest a role for *Dhx9* in the regulation of *Id2* expression. Consistently, the promoter region of -172 to -704 base pairs (bp) showed notable luciferase activity with *Dhx9* overexpression (Fig. 6F). To determine which domain of *Dhx9* is responsible for the binding to *Id2* promoter region, we constructed diverse vectors consisting of distinct truncated domains together with HA tag and performed immunoprecipitation and luciferase assay. The data showed that the OB_Fold domain is required for *Dhx9* binding to *Id2* promoter region (Fig. 6G). ChIP-seq and ATAC-seq data also showed distinct peaks at the *Acsbg1* and *Pde2a* loci (fig. S19, A and B). We further confirmed the regulation of *Dhx9* on *Acsbg1* and *Pde2a* genes using KO and overexpression approaches (fig. S19C) and further demonstrated that the OB_Fold domain is necessary for *Dhx9* binding to *Acsbg1* and *Pde2a* loci using luciferase reporter assay (fig. S19, D to F).

In addition to direct binding, *Dhx9* may also mediate the activation of target genes through locus opening and up-regulation of transcription activity in the absence of high-quality binding peaks by *Dhx9* (fig. S20A), as demonstrated in the top 15 genes shared by RNA-seq and ChIP-seq analyses (fig. S20, B and C). Yet, it remains to be further characterized whether those genes are required for the differentiation of CD8⁺ effector cells.

To determine whether *Id2* is responsible for *Dhx9*-mediated effector T cell differentiation, we transferred *Dhx9*^{-/-} OT-1 cells with or without *Id2* overexpression into WT recipients, followed by LM-OVA infection. Adoptive transfer of *Dhx9*^{-/-} cells overexpressing *Id2* rescued the percentage of CD44⁺CD62L⁻ cells following LM-OVA challenge (fig. S21, A and B). Since *Id2* is known to regulate lymphocyte differentiation through suppression of E-protein activity (39), we sought to determine the role of E2A protein, a member of the E-protein family, in *Dhx9*^{-/-} T cells using CD4Cre⁺*Dhx9*^{fl/fl}E2A^{fl/fl} mice. Following infection, we found that E2A deletion rescued the percentage of CD44⁺CD62L⁻ cells (Fig. 6, H and I) and KLRG1⁺IL-7R⁻ cells (Fig. 7, J and K) in *Dhx9*^{-/-} mice to levels comparable to control samples. Therefore, *Dhx9* regulates effector differentiation of CD8⁺ T cells through direct binding to the *Id2* promoter and enhancing *Id2* gene transcription.

Enhanced expression of *Dhx9* in effector CD8⁺ T cells from healthy individuals and COVID-19 patients

To explore the potential function of *Dhx9* in human immunity, we first evaluated *Dhx9* expression in naïve and activated human CD8⁺

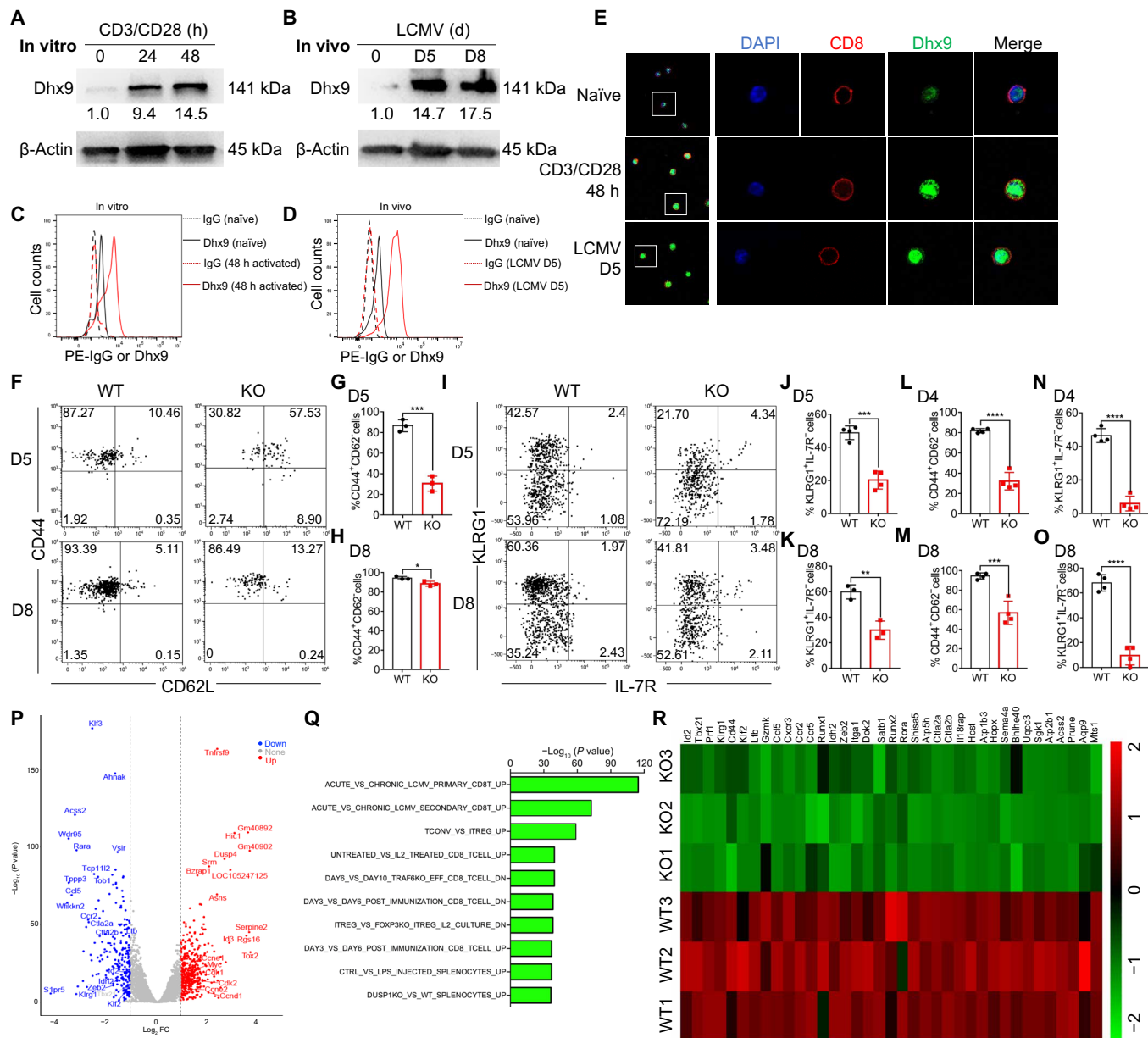


Fig. 5. Impaired effector differentiation of CD8⁺ T cells in Dhx9-deficient mice. Protein levels of Dhx9 measured by Western blot in CD8⁺ T cells stimulated with anti-CD3/anti-CD28 Abs for 24 and 48 hours (A) from WT mice 5 and 8 days after LCMV infection (B). Dhx9 expression measured by flow cytometry in CD8⁺ T cells stimulated with anti-CD3/anti-CD28 Abs for 48 hours (C) from WT mice infected with LCMV for 5 days (D). (E) Representative immunofluorescence staining of CD8 (red), Dhx9 (green), and nuclei [4',6-diamidino-2-phenylindole (DAPI)] in naïve, activated, and effector CD8⁺ T cells. Scale bars, 10 μ m. Representative FACS plots and percentages of CD44 and CD62L (F to H) and KLRG1 and IL-7R (I to K) in GP33⁺CD8⁺ T cells from mice 5 and 8 days after LCMV infection. (L to O) WT (CD45.1) and KO (CD45.2) CD8⁺ T cells were mixed at a 2:3 ratio with naïve CD4⁺ T cells and transferred into WT recipient mice (CD45.1⁺CD45.2⁻, 4.5-Gy irradiation), followed by LCMV infection. Splenocytes were analyzed for CD44 and CD62L (L and M) and KLRG1 and IL-7R (N and O) expression in GP33⁺CD8⁺ T cells 4 and 8 days after infection by FACS ($n = 3$ to 4 mice per group). (P) Volcano plot depicting \log_2 (fold change (FC)) (x axis) and $-\log_{10}$ (P value) (y axis) for differentially expressed genes (abs. \log_2 FC > 1, false discovery rate < 0.05) in splenic GP33⁺CD8⁺ T cells from mice following LCMV infection (day 8); up-regulation (red) and down-regulation (green) ($n = 3$ for each group). (Q) Gene set enrichment analysis for genes down-regulated with canonical pathways and immunologic signatures. Enrichment score value equals $-\log_{10}$ (P value). (R) Heatmap of representative down-regulated genes related to the pathway associated with effector T cells. The scale ranges from minimum (green) to medium (black) to maximum (red) relative expression. Data are representative of at least three independent experiments shown as the means \pm SEM. Statistical testing is depicted as two-sided, unpaired t tests; * $P \leq 0.05$; ** $P \leq 0.01$; *** $P \leq 0.001$; **** $P \leq 0.0001$.

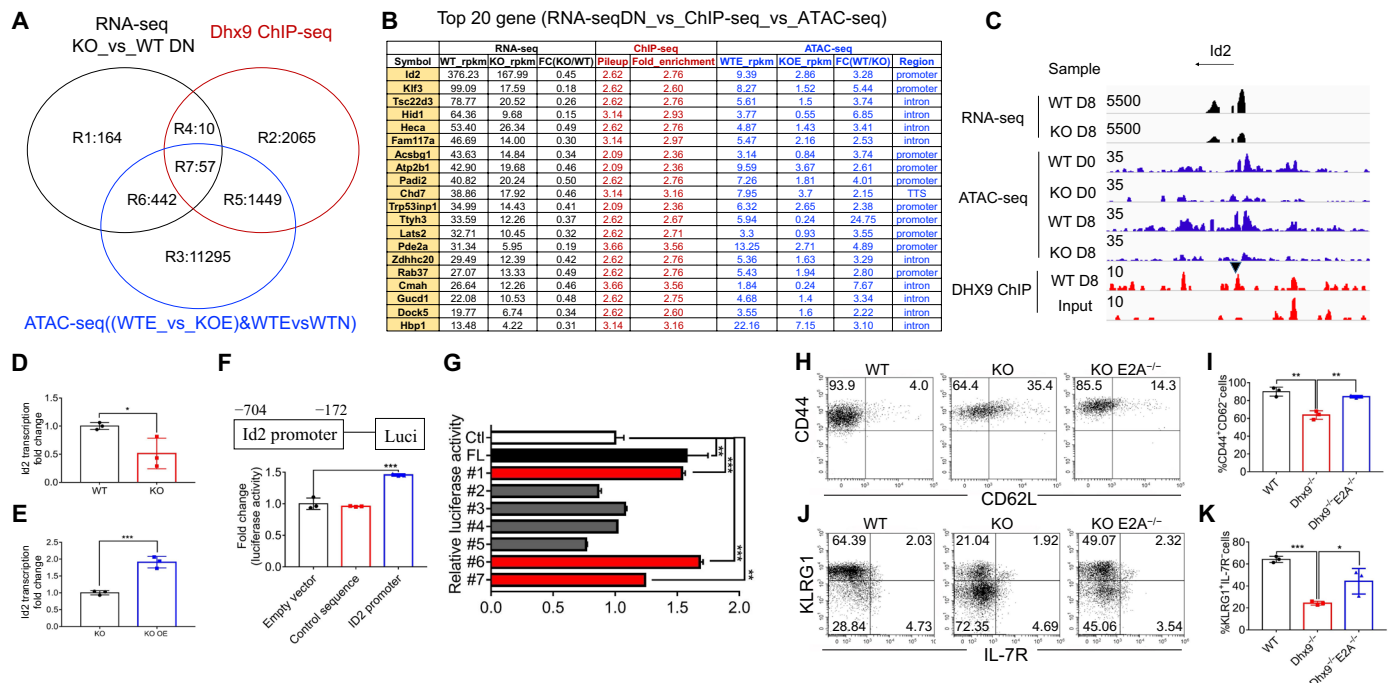


Fig. 6. *Id2* as a direct target of *Dhx9* for regulating effector CD8⁺ T cell differentiation. (A) Venn diagram depicting the overlapping portion of differentially expressed genes from RNA-seq (black), *Dhx9*-binding regions in ChIP-seq (red), and active accessible regions in ATAC-seq (blue). (B) Top 20 genes shared by RNA-seq, ChIP-seq, and ATAC-seq screens. (C) Alignments for *Id2* mRNA expression in effector CD8⁺ T cells with LCMV infection at day 8 (top), ATAC-seq peaks in the *Id2* locus of naive and effector CD8⁺ T cells (middle), and ChIP-seq peaks in *Id2* locus of WT cells compared with input. (D) mRNA levels of *Id2* in GP33⁺CD8⁺ T cells from WT or KO mice infected with LCMV for 5 days that were measured by qPCR. (E) *Dhx9*-deficient EL4 cell line, established by CRISPR-Cas9 technology using the sgRNA (single guide RNA) sequence (GAGGTTCGATTGCCCTTTGCAAGG), was infected with *Dhx9*-overexpressing retrovirus for 48 hours. The mRNA levels of *Id2* were measured by qPCR. (F) Schematic representation of *Id2* promoter region and luciferase reporter analysis for *Id2* promoter activity. The fragments (−172 to 702 bp) of *Id2* promoter or control sequence were cloned into the pGL4.16 plasmid, which were transfected into 293T cells together with MSCV-*Dhx9* vector. (G) Luciferase assay for the binding of different domains of *Dhx9* on the promoter region of *Id2* gene. (H to K) WT, CD4Cre⁺*Dhx9*^{fl/fl} (KO), and CD4Cre⁺*Dhx9*^{fl/fl}*E2A*^{fl/fl} (KO *E2A*^{-/-}) mice were infected with LCMV for 8 days. Splenocytes were analyzed for CD44 and CD62L (H) and KLRG1 and IL-7R (J) expression by FACS. Percentage of CD44⁺CD62L⁻ cells (I) and KLRG1⁺IL-7R⁻ cells (K) in GFP⁺CD8⁺ T cells (*n* = 3 mice per group). Data are representative of at least three independent experiments shown as the means ± SEM. Statistical testing is depicted as two-sided, unpaired *t* tests; **P* ≤ 0.05; ***P* ≤ 0.01; ****P* ≤ 0.001.

T cells. Human naïve CD8⁺ T cells can be characterized as CD8⁺CD45RA⁺CD45RO⁻CD25⁻ and become CD45RA⁺CD25⁺ activated or effector cells upon antigen stimulation. We thus stimulated naïve CD8⁺ T cells with anti-CD3 and anti-CD28 Abs for 48 hours. Western blotting showed that the protein level of *Dhx9* markedly increased after stimulation (Fig. 7A). Furthermore, flow cytometry [fluorescence-activated cell sorting (FACS)] analysis of CD25⁺CD8⁺ T cells displayed a higher level of *Dhx9* compared to CD45RA⁺CD45RO⁻CD25⁻ cells, as indicated by elevated mean fluorescence intensity (MFI) (Fig. 7, B and C) and percentage (Fig. 7D).

We further explored the potential role of *Dhx9* in coronavirus disease 2019 (COVID-19) based on the single-cell data from the published Gene Expression Omnibus (GEO) database (40). Our single-cell data analysis included a total of four healthy controls (HC1 to HC4) and nine COVID-19 patients, in which three patients had moderate symptoms (M1 to M3) and six patients had severe infections (S1 to S6). After removing the low-quality single-cell data, we obtained a total of 65,706 bronchoalveolar immune cells (21,792 for healthy controls, 7266 for moderate patients, and 36,648 for severe patients).

First, clustering analysis revealed 42 cell populations across all patients (fig. S25A). Furthermore, T cell population was extracted for further analysis using the marker genes including CD3E, CD3G,

and CD3D (fig. S25B). We extracted 9370 T cells and performed unbiased clustering using highly variable genes to reveal 15 clusters of T cell populations (Fig. 7E), most of which were largely different between healthy individuals and patients and between the patients with moderate and severe symptom (Fig. 7F). After the definition of CD4⁺ T and CD8⁺ T cells (Fig. 7G), we subsequently annotated seven functional CD8⁺ T cell clusters using previously described marker genes (41, 42): central memory (TCM), effector early (Eff_early), effector cycling (Eff_cycling), effector memory (TEM), tissue-resident memory (TRM), precursor exhausted (Tpex), and exhausted (Tex) (Fig. 7H). The data showed that DHX9 was found only highly expressed in Eff_cycling CD8 T cells (Fig. 7I). Notably, the expression of DHX9 in Eff_cycling CD8 T cells was higher in moderate than severe COVID-19 patients (Fig. 7J), indicating a correlation between DHX9 expression and potential antiviral ability in COVID-19 patients.

DISCUSSION

In the current study, we demonstrate that *Dhx9* is essential for activated CD8⁺ T cell survival and effector differentiation during viral infection. We found that loss of *Dhx9* triggered apoptosis of activated CD8⁺ T cells even before proliferation. Mechanistically, *Dhx9* serves as a key component of TCR signaling in CD8⁺ T cells by promoting

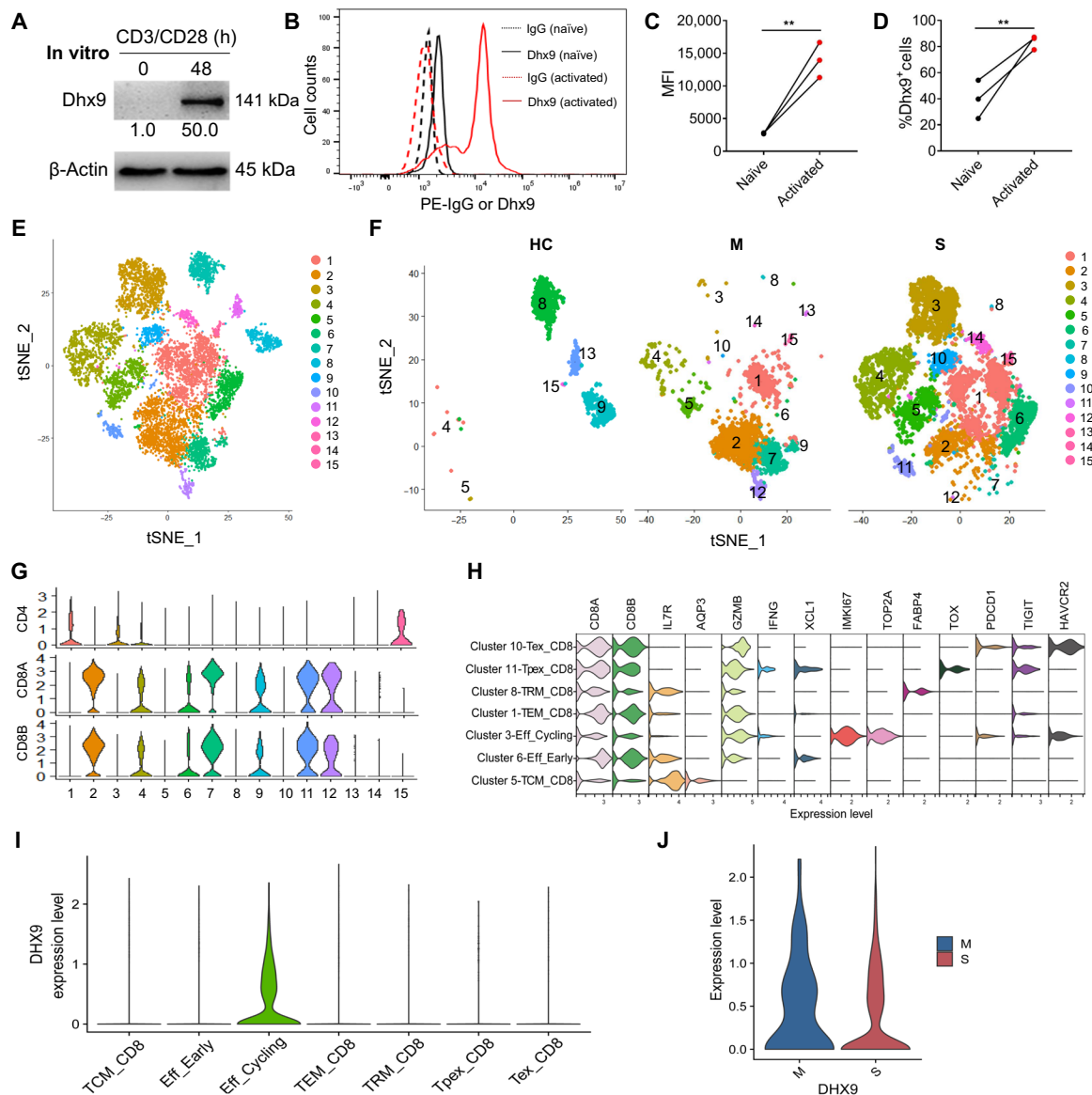


Fig. 7. Enhanced expression of Dhx9 in effector CD8⁺ T cells from healthy controls or virus-infected patients. (A to D) Peripheral blood mononuclear cells from healthy human donor were stimulated with anti-CD3 and anti-CD28 Abs for 48 hours. (A) The protein levels of Dhx9 in naïve (CD45RA⁺CD45RO⁻CD25⁻) or activated (CD25⁺) CD8⁺ cells were measured by Western blot. The protein levels were quantified and normalized to β-actin. (B) Representative FACS plots of Dhx9 staining. Black dashed line [immunoglobulin G (IgG) isotype control, naïve], red dashed line (IgG isotype control, activated), black solid line (Dhx9 Ab, naïve), and red solid line (Dhx9 Ab, activated). (C) MFI of Dhx9 expression in naïve CD8⁺ cells and activated CD8⁺ cells. (D) Percentage of Dhx9⁺ cells in naïve and activated CD8⁺ cells (*n* = 3 wells per group). (E) tSNE plot of the distribution of all bronchoalveolar lavage fluid (BALF) T cells in COVID-19 patients, colored by different clusters. (F) tSNE projections of BALF T cells among healthy controls (HC) and patients with moderate (M) and severe (S) symptom with COVID-19 infection. (G) Violin plots comparing the expression levels of representative T cell marker genes among different clusters. (H) Violin plots comparing the expression levels of representative marker genes among different sub-CD8⁺ T cell clusters. (I) Violin plots comparing the expression levels of DHX9 among different sub-CD8⁺ T cell clusters. (J) Violin plots comparing the expression levels of DHX9 in Eff_cycling CD8⁺ T cells between patients with moderate and severe disease. The gene expression in (G) to (J) is represented as expression of normalized log₂ (count + 1).

LCK-mediated ZAP70 phosphorylation and ERK activation to ensure T cell survival during early activation stage. In addition, Dhx9 controls effector differentiation of CD8⁺ T cells by directly regulating *Id2* transcription. Therefore, we uncovered a previously undefined role of a nuclear sensor, Dhx9, in CD8⁺ T cell survival, effector differentiation, and antiviral response.

Upon viral infection, CD8⁺ T cell proliferation and apoptosis are tightly controlled and often occur in parallel during TCR stimulation.

Of note, we show that Dhx9 is absolutely required for activated CD8⁺ T cell survival. Loss of Dhx9 led to increased cell death accompanied by enhanced Bim expression and reduced Bcl-2 expression (Fig. 2K). We found that loss of Dhx9 caused immediate apoptosis of activated CD8⁺ T cells before or at the beginning of proliferation. Given that Egr1 is the immediate early response gene downstream of ERK, it is possible that ERK controls effector CD8⁺ T cell survival through the Egr1 gene family. However, Egr1 did not affect antigen-specific

CD8⁺ T cell expansion (43) and survival (fig. S22, A and B). It was previously shown that p38 and JNK induce CD8⁺ T cell death, while ERK promotes cell survival by enhancing the phosphorylation and proteasome-dependent degradation of Bim (44–47). Consistently, our in vitro data showed that inhibition of either JNK or ERK led to an increase of apoptosis, while only treatment with an ERK agonist rescued Dhx9^{-/-} cells from cell death (Fig. 3, A to D). These findings suggest that Dhx9 regulates cell survival via the ERK-Bim axis independent of Egr1, which is in line with down-regulated phosphorylated ERK level in Dhx9^{-/-} cells. Moreover, we provide compelling evidence that the DSRM domain of Dhx9 is critically required for the survival of activated CD8⁺ T cells. Furthermore, our MS data showed that DHX9 could bind to LCK (Fig. 4A), and immunoprecipitation experiment demonstrated that DHX9 formed a complex with CD3ε, LCK, and ZAP70 (Fig. 4, C and D). The reduction of pZAP70 expression and decreased binding between LCK and ZAP70 in Dhx9^{-/-} cells support the requirement of Dhx9 for LCK-mediated ZAP70 phosphorylation (Fig. 4E). Together, Dhx9 transduces signals through LCK-ZAP70-ERK downstream of TCR activation and prevents activated CD8⁺ T cells from immediate apoptosis.

Dhx9 is able to regulate gene transcription at the chromosomal or single-gene level by unwinding double strands of DNA and RNA (48–53). Using RNA-seq and ATAC-seq, we demonstrate that Dhx9 regulates the expression of a cluster of well-defined genes required for CD8⁺ T cell effector differentiation (Fig. 5R). ChIP-seq data analysis suggests that Dhx9 directly binds to *Id2*, a key transcriptional factor for effector differentiation (Fig. 6C). It is possible that Dhx9 regulates *Id2* expression through the LCK-ZAP70-ERK-Egr1 axis downstream of TCR signaling, as Dhx9^{-/-} cells displayed down-regulation of ERK and Egr1, but not Egr2 and Egr3 (fig. S7B), a decrease of *Id2* expression in activated Egr1^{-/-} CD8⁺ T cells (fig. S24A), and a mild binding of Egr1 to *Id2* promoter region (fig. S24B). Egr1 overexpression was unable to rescue *Id2* expression (fig. S24, C to E) in Dhx9^{-/-} cells, strongly suggesting that Dhx9 controls effector CD8⁺ T cell fate by regulating *Id2* transcription independent of Egr1 function. In addition, we detected several other genes involved in effector functions, although they do not directly interact with Dhx9 (fig. S17). It is likely that Dhx9 behaves as a transcription factor rather than a nuclear helicase, since we did not observe an increased transcription of neighboring genes of *Id2* (fig. S23). The defects of CD8⁺ T cell effector differentiation are likely due to dysregulated expression of *Id2* and other effector-related genes. Together, these observations suggest that Dhx9 may regulate multiple target genes either directly or indirectly to facilitate the effector differentiation program. Future studies are definitely required to assess the functions of other candidate genes beyond *Id2*.

Together, our study suggests that the nuclear helicase Dhx9 plays a crucial role in CD8⁺ T cell immunity against viral infection by protecting from cell death at the immediate-early activation stage and promoting effector differentiation at a later stage. We revealed a previously unknown mechanism of Dhx9 to control CD8⁺ T cell survival and effector differentiation by directly regulating TCR signaling and *Id2* transcription. We further described a potential role for Dhx9 in CD8⁺ T cells during immune defense against severe acute respiratory syndrome coronavirus disease 2 (SARS-CoV-2). Our findings highlight the significance of cell survival at early activation stage even before proliferative burst for CD8⁺ T cell-mediated immunity.

MATERIALS AND METHODS

Mice

C57BL/6J, CD45.1, OT-1, Egr1^{-/-}, and Rag2^{-/-} mice were purchased from The Jackson Laboratory. CD4Cre transgenic mice on the C57BL/6J background were purchased from Taconic Biosciences. The generation of Dhx9^{fl/fl} strain is illustrated in fig. S1A. Mice harboring the T cell-specific Dhx9 deletion (CD4Cre⁺Dhx9^{fl/fl}) were generated by crossing Dhx9^{fl/fl} mice to CD4Cre⁺ mice. All procedures were approved by the Institutional Animal Care and Use Committee of Xi'an Jiaotong University, Xi'an Center for Disease Control, and Suzhou Institute of Systems Medicine.

Abs and flow cytometry

The monoclonal Abs that were used to stain cells in the flow cytometry analyses were as follows: anti-mouse CD8a (53-6.7), anti-mouse CD4 (GK1.5), anti-mouse CD44 (IM7), anti-mouse 62L (MEL-14), anti-mouse KLRG1 (2F1/KLRG1), anti-mouse IL-7R (A7R34), anti-mouse IL-2 (JE56-5H4), anti-mouse IFN-γ (XMG1.2), and phycoerythrin (PE) donkey anti-rabbit immunoglobulin G (IgG) (Poly4064) and PE anti-mouse Ki-67 (16A8). All these antibodies were purchased from BioLegend. The fluorescein isothiocyanate (FITC) BrdU Flow Kit and 7-aminoactinomycin D (7AAD) were purchased from BD Biosciences.

For intracellular cytokine staining, splenocytes and lymph node cells were stimulated for 4 hours in vitro with phorbol 12-myristate 13-acetate (PMA)/ionomycin in the presence of monensin and brefeldin A. The stimulated cells were fixed and permeabilized using a Fixation/Permeabilization Solution kit (BioLegend). Cells were analyzed using a CytoFLEX flow cytometer (Beckman Coulter). CytExpert software was used for data analysis. Naïve (CD62L⁺CD44⁻) and effector (CD62L⁻CD44⁺) CD8⁺ T cells were sorted with BD FACSAria (BD Biosciences).

Quantitative PCR

The RNeasy Mini Kit (QIAGEN) was used to extract total RNA from purified T cells according to the manufacturer's instruction. Complementary DNA (cDNA) was synthesized using the cDNA Synthesis Kit (TOYOBO). qPCR was performed based on the StepOnePlus Real-Time PCR System (Thermo Fisher Scientific) using SYBR Green RT-qPCR Master Mix (GenStar). The primers used in this study were listed in table S5.

Western blotting

Purified CD8⁺ T cells were lysed in radioimmunoprecipitation assay (RIPA) lysis buffer (Beyotime Biotechnology) to extract the total proteins. Samples were separated on SDS-polyacrylamide gels and electrotransferred onto polyvinylidene fluoride membranes (Millipore). After blocking with 5% skimmed milk, membranes were incubated with indicated primary Abs at 4°C overnight, followed by incubation with secondary Abs at room temperature for 1 hour. The protein expression was measured by FUSION Solo.6 s (Vilber).

LCMV and LM infection

LCMV-Armstrong was propagated in BHK-21 cells. The viral titers were determined using plaque assays in Vero cells. In the LCMV infection model, mice were infected with 2 × 10⁵ plaque-forming units (PFUs) of Armstrong-LCMV intraperitoneally. In the LM infection model, mice were infected with 2 × 10⁵ (sublethal) or 5 × 10⁵ (lethal) CFUs of LM intravenously. The splenocytes were analyzed on the indicated days after infection.

T cell adoptive transfer

Single-cell suspensions were prepared from the spleens and/or lymph nodes. Naïve CD8⁺ T cells from WT (CD45.1⁺) and Dhx9^{fl/fl}CD4Cre⁺ (CD45.2⁺) mice were mixed at a ratio of 2:3 and transferred intravenously into age- and sex-matched, sublethally irradiated (4.5-Gy) WT mice (CD45.1⁺CD45.2⁺). Twenty-four hours after cell transfer, recipient mice were infected intraperitoneally with 2×10^5 PFU of Armstrong-LCMV. Splenocytes were collected and analyzed for cell surface markers and cytokines by flow cytometry.

Ex vivo analysis of T cells

Single cells were obtained from the spleen, lymph node, or blood. For cell surface staining, a total of 1×10^6 to 5×10^6 cells were stained in the dark at 4°C for 30 min. For intracellular cytokine staining, splenocytes were stimulated for 4 hours in vitro with PMA (50 ng/ml) and ionomycin (1 µg/ml) in the presence of monensin and brefeldin A. Stimulated cells were fixed and permeabilized using the Fixation/Permeabilization Solution Kit (BioLegend). Cells were analyzed on a CytoFLEX flow cytometer (Beckman Coulter). The data were analyzed with FlowJo software (TreeStar or CytExpert).

To examine in vivo proliferation, 100 µl (10 mg/ml) of BrdU per mouse was injected intraperitoneally 4 hours before collection. For in vitro proliferation, cells were labeled with 5 µM carboxyfluorescein diacetate succinimidyl ester (CFSE), followed by three washes, and stimulated with anti-CD3 (5 µg/ml) and anti-CD28 (2 µg/ml) Abs for 48 or 72 hours. Alternatively, cells were stimulated with anti-CD3 (5 µg/ml) and anti-CD28 (2 µg/ml) Abs for 48 or 72 hours, followed by the addition of 10 mM BrdU 30 min before cell collection. Samples were treated with the FITC BrdU Flow Kit (BD Biosciences) or Ki67 Ab for staining followed by flow cytometry analysis.

For apoptosis assays, freshly isolated or in vitro cultured (24, 48, or 72 hours) cells were stained with indicated surface markers, followed by washing with FACS buffer [1× phosphate-buffered saline (PBS) with 1% fetal bovine serum]. Apoptosis was detected using the 7AAD/Annexin V Apoptosis Detection Kit (BD Biosciences). Samples were collected using a CytoFLEX flow cytometer (Beckman Coulter).

Retroviral production and transduction

Retrovirus was produced by transfecting 2.4 µg of each retroviral vector in combination with 0.3 µg of pCL-Eco retrovirus packaging vector into six-well plates with cultured BOSC 23 cells using jetPRIME transfection reagent (Polyplus). Following 48 and 72 hours, the culture supernatant containing retrovirus was collected through 0.45-µm filters. Purified CD8⁺ T cells were stimulated overnight using plate-bound anti-CD3 (5 µg/ml) and anti-CD28 Abs (2 µg/ml) or concanavalin A (2.5 µg/ml). Spin infection of stimulated T cells using retrovirus supernatant was performed at 2500 rpm for 90 min at 37°C. Green fluorescent protein-positive (GFP⁺) cells were examined using flow cytometry analysis or sorted for in vitro or in vivo experiments.

Luciferase assay

The DNA fragments were cloned into the pGL4.16 (luc2CP/Hgro) vector (Promega), which contains the luciferase reporter gene luc2CP. The pGL4.16 plasmid and control vector pGL4.74 (hRluc/TK) encoding the luciferase reporter gene hRluc (*Renilla reniformis*), along with plasmids expressing candidate genes, were transfected into 293T cell lines (American Type Culture Collection). Forty-eight hours

after transfection, the luciferase activity of both Firefly luciferase and Renilla luciferase was measured with a Dual-Luciferase Reporter kit (Promega) on a Synergy Neo2 Multi-Mode reader (BioTek).

RNA-seq library preparation and sequencing

CD44⁺CD62⁻ effector CD8⁺ T cells were sorted from the spleens of LCMV-Armstrong-infected CD4Cre⁺Dhx9^{fl/fl} mice and WT littermates. Total RNA was extracted using the RNeasy Mini Kit (QIAGEN) according to the manufacturer's protocol. RNA concentration was detected by the Qubit RNA broad range assay in the Qubit Fluorometer (Invitrogen). After quality control using ribonuclease-free agarose gel and Agilent 2100 (Agilent Technologies, Palo Alto, CA, USA), RNA-seq libraries were prepared using 200 ng of total RNA with a TruSeq RNA Sample Preparation kit (Illumina). Oligo(dT)-enriched mRNAs were fragmented randomly with fragmentation buffer, followed by first- and second-strand cDNA synthesis. After a series of terminal repair, the double-stranded cDNA library was obtained through PCR enrichment and size selection. The prepared cDNA library was sequenced with the Illumina HiSeq 2000 sequencer (Illumina HiSeq 2000 v4 Single-Read 50 bp) after pooling according to its expected data volume and effective concentration.

Three biological replicates were performed in RNA-seq analysis. Raw reads were mapped against the mouse genome (GRCm38) using TopHat2 RNA-seq alignment software, and unique reads were retained to quantify gene expression counts from TopHat2 alignment files. Data were analyzed and preprocessed in the R environment. Differential expression analysis was performed using R package DESeq2 (adjusted $P < 0.05$ and fold change > 1.5). Heat maps and volcano plots were visualized using the R package.

ChIP-seq library preparation and sequencing

CD44⁺CD62⁻ effector CD8⁺ T cells were sorted from LCMV-Armstrong-infected WT mice by BD FACSAria flow cytometry (BD Biosciences). Anti-Dhx9 Ab (Abcam) and Millipore 17-10085 ChIP kit were used in ChIP. Immunoprecipitated DNA was used for Illumina ChIP-seq sample preparation. In brief, 5×10^7 cells were crosslinked to chromatin with 1% formaldehyde. Reaction was stopped with 0.125 M glycine. Cells were resuspended in cold nuclear lysis buffer and sonicated to ~300- to 500-bp size, followed by precipitation with immunoprecipitation-grade anti-Dhx9 and magnetic protein A/G beads overnight. The following day, beads were washed by low-salt, high-salt, LiCl, and TE (tris-EDTA) buffers. Bound complexes were eluted in 150 µl of elution buffer at 62°C for 2 hours with shaking, followed by reversal of formaldehyde crosslinking at 95°C for 10 min. DNA was purified with spin columns.

Immunoprecipitated DNA concentration was detected by the Qubit DNA broad range assay in the Qubit Fluorometer (Invitrogen). Ten nanograms of immunoprecipitated DNA was prepared for sequencing using the Illumina ChIP-seq sample preparation protocol. Blunt-end DNA fragments were ligated to Illumina adaptors, amplified, and sequenced using a NovaSeq 6000 sequencer (Illumina) with PE150 model. Raw sequencing data were filtered by Trimmomatic (version 0.36). FastQ reads were aligned to the ensemble mouse genome (GRCm38) with STAR software (version 2.5.3a) using default settings. The MACS2 software (version 2.1.1) was used to process peak calling. Genomic graphs were generated and viewed with the IGV (Integrative Genomics Viewer).

ATAC-seq library preparation and sequencing

Naive CD8⁺ T cells (CD44⁺CD62⁺) (5×10^4) were sorted from CD4Cre⁺Dhx9^{fl/fl} mice and WT littermates. Effector CD8⁺ T cells (CD44⁺CD62⁻) (5×10^4) were sorted from LCMV-Armstrong-infected CD4Cre⁺Dhx9^{fl/fl} mice and WT littermates on day 8 after infection. Purified cells were washed in cold PBS and lysed using ATAC-seq lysis buffer [10 mM tris-HCl (pH 7.4), 10 mM NaCl, 3 mM MgCl₂, and NP-40] on ice for 10 min. Nuclei suspensions were incubated in transposition mix buffer, which includes 2.5 μl of Nextera Tn5 transposase at 37°C for 30 min. Immediately following transposition, the transposed DNA fragments were purified using a QIAGEN MiniElute kit, amplified as described (54), and sequenced using Illumina HiSeq 4000 with 30 million pairs. After filtering the raw reads containing adapters or low-quality bases, 50-bp paired-end ATAC-seq clean reads from each sample were aligned to the ensemble mouse genome (GRCm38) with bowtie using Bowtie2 (version 2.2.8) (55). For all data files, duplicates were removed using Picard. ATAC-seq peak regions were called by MACS (version 2.1.2) with parameters “--nomodel --shift -100 --extsize 200 -B -q 0.05” and filtered to remove putative copy number altered regions (56).

Immunoprecipitation and MS

CD44⁺CD62⁻ CD8⁺ T cells (5×10^7) were sorted from the spleens of LCMV-Armstrong-infected C57BL/6J mice and lysed in RIPA lysis buffer (Beyotime Biotechnology) supplemented with 1% phenylmethylsulfonyl fluoride on ice for 30 min. Anti-Dhx9 Abs or normal mouse IgG (Millipore) was added into the samples followed by a 4-hour rotation at 4°C. Samples were then incubated with magnetic protein A/G beads (Millipore) at 4°C overnight. After several washes with tris-NaCl buffer [20 mM tris (pH 7.4) and 120 mM NaCl], immunoprecipitated proteins were released from beads with lysis buffer and 6× loading buffer at 95°C for 10 min and applied to SDS-polyacrylamide gel.

For in-gel tryptic digestion, gel pieces were processed by the following steps: (i) destained in 50 mM NH₄HCO₃ in 50% acetonitrile (v/v) until clear, (ii) dehydrated with 100 μl of 100% acetonitrile for 5 min, (iii) rehydrated in 10 mM dithiothreitol at 56°C for 60 min, (iv) dehydrated in 100% acetonitrile, (v) rehydrated with 55 mM iodoacetamide at room temperature in the dark for 45 min, (vi) washed with 50 mM NH₄HCO₃ and dehydrated with 100% acetonitrile, (vii) rehydrated with trypsin (10 ng/μl) and resuspended in 50 mM NH₄HCO₃ on ice for 1 hour, and (viii) digested with trypsin at 37°C overnight. Peptides were extracted with 50% acetonitrile/5% formic acid, followed by 100% acetonitrile, dried to completion, and resuspended in 2% acetonitrile/0.1% formic acid.

For liquid chromatography-MS/MS analysis, on an EASY-nLC 1000 ultra-performance liquid chromatograph (UPLC) system, the tryptic peptides were dissolved in 0.1% formic acid and directly loaded onto a homemade reversed-phase analytical column (15-cm length, 75-μm inside diameter). The gradient was composed of an increasing concentration of 6 to 23% solvent B (0.1% formic acid in 98% acetonitrile) over 16 min, 23 to 35% in 8 min, and climbing to 80% in 3 min, and then holding at 80% for the last 3 min. The peptides were subjected to a nano spray ion (NSI) source followed by MS/MS in Q Exactive Plus (Thermo Fisher Scientific) coupled online to the UPLC. Intact peptides were detected in the Orbitrap at a resolution of 70,000. Peptides were then selected for MS/MS using the normalized collision energy (NCE) setting as 28, and the fragments were detected in the Orbitrap at a resolution of 17,500. The resulting MS/MS data were processed using Proteome Discoverer 1.3.

Single-cell RNA-seq data analysis

The data from a previous single-cell RNA-seq study of bronchoalveolar immune cells in patients with COVID-19 were reanalyzed (accession number GEO: GSE145926) (57). The gene expression matrices of all patients were imported into Seurat v3 (58) and merged for subsequent analyses. The following filtering steps were carried out to exclude low-quality cells: Cells with fewer than 200 and more than 6000 detected genes were discarded; cells with a high fraction of mitochondrial genes (>10%) are removed. As a result, a total of 65,706 cells with a median of 1523 genes were included in the analyses. The nonlinear dimensional reduction was performed with the *t*-distributed stochastic neighbor embedding (tSNE) method, and cluster biomarkers were found by the “Seurat” package.

Statistical analysis

Statistical analyses were applied to biologically independent mice or technical replicates for each experiment. Each experiment was independently repeated at least three times. Two-tailed Student's *t* test was used for all statistical calculations using GraphPad Prism 7 software. All bar graphs include means with error bars to show the distribution of the data. The level of significance is indicated as **P* < 0.05; ***P* < 0.01; ****P* < 0.001; *****P* < 0.0001.

SUPPLEMENTARY MATERIALS

Supplementary material for this article is available at <https://science.org/doi/10.1126/sciadv.abk2691>

[View/request a protocol for this paper from Bio-protocol.](#)

REFERENCES AND NOTES

- J. T. Chang, E. J. Wherry, A. W. Goldrath, Molecular regulation of effector and memory T cell differentiation. *Nat. Immunol.* **15**, 1104–1115 (2014).
- S. M. Kaech, W. Cui, Transcriptional control of effector and memory CD8⁺ T cell differentiation. *Nat. Rev. Immunol.* **12**, 749–761 (2012).
- S. M. Kaech, S. Hemby, E. Kersh, R. Ahmed, Molecular and functional profiling of memory CD8 T cell differentiation. *Cell* **111**, 837–851 (2002).
- M. A. Williams, M. J. Bevan, Effector and memory CTL differentiation. *Annu. Rev. Immunol.* **25**, 171–192 (2007).
- N. Zhang, M. J. Bevan, CD8(+) T cells: Foot soldiers of the immune system. *Immunity* **35**, 161–168 (2011).
- B. Youngblood, J. S. Hale, H. T. Kissick, E. Ahn, X. Xu, A. Wieland, K. Araki, E. E. West, H. E. Ghoneim, Y. Fan, P. Dogra, C. W. Davis, B. T. Konieczny, R. Antia, X. Cheng, R. Ahmed, Effector CD8 T cells dedifferentiate into long-lived memory cells. *Nature* **552**, 404–409 (2017).
- L. Zhang, B. O. Tschumi, I. C. Lopez-Mejia, S. G. Oberle, M. Meyer, G. Samson, M. A. Ruegg, M. N. Hall, L. Fajas, D. Zehn, J. P. Mach, A. Donda, P. Romero, Mammalian target of rapamycin complex 2 controls CD8 T cell memory differentiation in a foxo1-dependent manner. *Cell Rep.* **14**, 1206–1217 (2016).
- O. Acuto, F. Michel, CD28-mediated co-stimulation: A quantitative support for TCR signalling. *Nat. Rev. Immunol.* **3**, 939–951 (2003).
- H. Chi, Regulation and function of mTOR signalling in T cell fate decisions. *Nat. Rev. Immunol.* **12**, 325–338 (2012).
- J. S. Haring, V. P. Badovinac, J. T. Harty, Inflaming the CD8⁺ T cell response. *Immunity* **25**, 19–29 (2006).
- A. E. Denton, R. Wesselingh, S. Gras, C. Guillonnet, M. R. Olson, J. D. Mintern, W. Zeng, D. C. Jackson, J. Rossjohn, P. D. Hodgkin, P. C. Doherty, S. J. Turner, Affinity thresholds for naive CD8⁺ CTL activation by peptides and engineered influenza A viruses. *J. Immunol.* **187**, 5733–5744 (2011).
- S. Viganò, D. T. Utzschneider, M. Perreau, G. Pantaleo, D. Zehn, A. Harari, Functional avidity: A measure to predict the efficacy of effector T cells? *Clin. Dev. Immunol.* **2012**, 153863 (2012).
- D. Zehn, S. Y. Lee, M. J. Bevan, Complete but curtailed T-cell response to very low-affinity antigen. *Nature* **458**, 211–214 (2009).
- K. D. Omilusik, M. S. Nadjjsombati, L. A. Shaw, B. Yu, J. J. Milner, A. W. Goldrath, Sustained Id2 regulation of E proteins is required for terminal differentiation of effector CD8(+) T cells. *J. Exp. Med.* **215**, 773–783 (2018).
- A. Xin, F. Masson, Y. Liao, S. Preston, T. Guan, R. Gloury, M. Olshansky, J.-X. Lin, P. Li, T. P. Speed, G. K. Smyth, M. Ernst, W. J. Leonard, M. Pellegrini, S. M. Kaech, S. L. Nutt,

- W. Shi, G. T. Belz, A. Kallies, A molecular threshold for effector CD8(+) T cell differentiation controlled by transcription factors Blimp-1 and T-bet. *Nat. Immunol.* **17**, 422–432 (2016).
16. Y. Ji, Z. Pos, M. Rao, C. A. Klebanoff, Z. Yu, M. Sukumar, R. N. Reger, D. C. Palmer, Z. A. Borman, P. Muranski, E. Wang, D. S. Schrumpp, F. M. Marincola, N. P. Restifo, L. Gattinoni, Repression of the DNA-binding inhibitor Id3 by Blimp-1 limits the formation of memory CD8+ T cells. *Nat. Immunol.* **12**, 1230–1237 (2011).
 17. A. Kallies, A. Xin, G. T. Belz, S. L. Nutt, Blimp-1 transcription factor is required for the differentiation of effector CD8(+) T cells and memory responses. *Immunity* **31**, 283–295 (2009).
 18. R. L. Rutishauser, G. A. Martins, S. Kalachikov, A. Chandele, I. A. Parish, E. Meffre, J. Jacob, K. Calame, S. M. Kaech, Transcriptional repressor Blimp-1 promotes CD8(+) T cell terminal differentiation and represses the acquisition of central memory T cell properties. *Immunity* **31**, 296–308 (2009).
 19. H. Shin, S. D. Blackburn, A. M. Intlekofer, C. Kao, J. M. Angelosanto, S. L. Reiner, E. J. Wherry, A role for the transcriptional repressor Blimp-1 in CD8(+) T cell exhaustion during chronic viral infection. *Immunity* **31**, 309–320 (2009).
 20. S. Yao, B. F. Buzo, D. Pham, L. Jiang, E. J. Taparowsky, M. H. Kaplan, J. Sun, Interferon regulatory factor 4 sustains CD8(+) T cell expansion and effector differentiation. *Immunity* **39**, 833–845 (2013).
 21. M. Kurachi, R. A. Barnitz, N. Yosef, P. M. Odorizzi, M. A. Dilorio, M. E. Lemieux, K. Yates, J. Godec, M. G. Klatt, A. Regev, E. J. Wherry, W. N. Haining, The transcription factor BATF operates as an essential differentiation checkpoint in early effector CD8+ T cells. *Nat. Immunol.* **15**, 373–383 (2014).
 22. S. Akira, S. Uematsu, O. Takeuchi, Pathogen recognition and innate immunity. *Cell* **124**, 783–801 (2006).
 23. A. L. Blasius, B. Beutler, Intracellular toll-like receptors. *Immunity* **32**, 305–315 (2010).
 24. K. Honda, A. Takaoka, T. Taniguchi, Type I interferon [corrected] gene induction by the interferon regulatory factor family of transcription factors. *Immunity* **25**, 349–360 (2006).
 25. O. Takeuchi, S. Akira, Pattern recognition receptors and inflammation. *Cell* **140**, 805–820 (2010).
 26. T. Kim, S. Pazhoor, M. Bao, Z. Zhang, S. Hanabuchi, V. Facchinetti, L. Bover, J. Plumas, L. Chaperot, J. Qin, Y.-J. Liu, Aspartate-glutamate-alanine-histidine box motif (DEAH)/RNA helicase A helicases sense microbial DNA in human plasmacytoid dendritic cells. *Proc. Natl. Acad. Sci. U.S.A.* **107**, 15181–15186 (2010).
 27. Z. Zhang, B. Yuan, N. Lu, V. Facchinetti, Y. J. Liu, DHX9 pairs with IPS-1 to sense double-stranded RNA in myeloid dendritic cells. *J. Immunol.* **187**, 4501–4508 (2011).
 28. S. Zhang, F. Grosse, Nuclear DNA helicase II unwinds both DNA and RNA. *Biochemistry* **33**, 3906–3912 (1994).
 29. H. R. Koh, L. Xing, L. Kleiman, S. Myong, Repetitive RNA unwinding by RNA helicase A facilitates RNA annealing. *Nucleic Acids Res.* **42**, 8556–8564 (2014).
 30. S. Zhang, F. Grosse, Domain structure of human nuclear DNA helicase II (RNA helicase A). *J. Biol. Chem.* **272**, 11487–11494 (1997).
 31. Y. C. Ng, W.-C. Chung, H.-R. Kang, H.-J. Cho, E.-B. Park, S.-J. Kang, M. J. Song, A DNA-sensing-independent role of a nuclear RNA helicase, DHX9, in stimulation of NF- κ B-mediated innate immunity against DNA virus infection. *Nucleic Acids Res.* **46**, 9011–9026 (2018).
 32. S. Zhu, S. Ding, P. Wang, Z. Wei, W. Pan, N. W. Palm, Y. Yang, H. Yu, H.-B. Li, G. Wang, X. Lei, M. R. de Zoete, J. Zhao, Y. Zheng, H. Chen, Y. Zhao, K. A. Jurado, N. Feng, L. Shan, Y. Kluger, J. Lu, C. Abraham, E. Fikrig, H. B. Greenberg, R. A. Flavell, Nlrp9b inflammasome restricts rotavirus infection in intestinal epithelial cells. *Nature* **546**, 667–670 (2017).
 33. A. H. Rahman, D. K. Taylor, L. A. Turka, The contribution of direct TLR signaling to T cell responses. *Immunol. Res.* **45**, 25–36 (2009).
 34. J. M. Reynolds, C. Dong, Toll-like receptor regulation of effector T lymphocyte function. *Trends Immunol.* **34**, 511–519 (2013).
 35. T. Uchimura, Y. Oyama, M. Deng, H. Guo, J. E. Wilson, E. Rampanelli, K. D. Cook, I. Misumi, X. Tan, L. Chen, B. Johnson, J. Tam, W.-C. Chou, W. J. Brickey, A. Petrucelli, J. K. Whitmire, J. P. Y. Ting, The innate immune sensor NLR3 acts as a rheostat that fine-tunes T cell responses in infection and autoimmunity. *Immunity* **49**, 1049–1061.e6 (2018).
 36. F. Salerno, A. Guislain, D. Cansever, M. C. Wolkers, TLR-mediated innate production of IFN- γ by CD8+ T cells is independent of glycolysis. *J. Immunol.* **196**, 3695–3705 (2016).
 37. F. Salerno, J. J. Freen-van Heeren, A. Guislain, B. P. Nicolet, M. C. Wolkers, Costimulation through TLR2 drives polyfunctional CD8(+) T cell responses. *J. Immunol.* **202**, 714–723 (2019).
 38. Y. Zhu, S. Liu, Q. Yin, T. Xu, X. Wu, Y. Zhuang, Generation of Dhx9-deficient clones in T-cell development with a mitotic recombination technique. *Genesis* **50**, 543–551 (2012).
 39. M. W. Quong, W. J. Romanow, C. Murre, E protein function in lymphocyte development. *Annu. Rev. Immunol.* **20**, 301–322 (2002).
 40. M. Liao, Y. Liu, J. Yuan, Y. Wen, G. Xu, J. Zhao, L. Cheng, J. Li, X. Wang, F. Wang, L. Liu, I. Amit, S. Zhang, Z. Zhang, Single-cell landscape of bronchoalveolar immune cells in patients with COVID-19. *Nat. Med.* **26**, 842–844 (2020).
 41. A. Kusnadi, C. Ramirez-Suastegui, V. Fajardo, S.-J. Chee, B. J. Meckiff, H. Simon, E. Pelosi, G. Seumois, F. Ay, P. Vijayanand, H. H. Ottensmeier, Severely ill patients with COVID-19 display impaired exhaustion features in SARS-CoV-2-reactive CD8+ T cells. *Sci. Immunol.* **6**, eabk4782 (2021).
 42. M. Andreatta, J. Corria-Osorio, S. Müller, R. Cubas, G. Coukos, S. J. Carmona, Interpretation of T cell states from single-cell transcriptomics data using reference atlases. *Nat. Commun.* **12**, 2965 (2021).
 43. A. Singh, J. Svaren, J. Grayson, M. Suresh, CD8 T cell responses to lymphocytic choriomeningitis virus in early growth response gene 1-deficient mice. *J. Immunol.* **173**, 3855–3862 (2004).
 44. C. Merritt, H. Enslin, N. Diehl, D. Conze, R. J. Davis, M. Rincón, Activation of p38 mitogen-activated protein kinase in vivo selectively induces apoptosis of CD8(+) but not CD4(+) T cells. *Mol. Cell. Biol.* **20**, 936–946 (2000).
 45. K. Sabapathy, T. Kallunki, J.-P. David, I. Graef, M. Karin, E. F. Wagner, c-Jun NH2-terminal kinase (JNK)1 and JNK2 have similar and stage-dependent roles in regulating T cell apoptosis and proliferation. *J. Exp. Med.* **193**, 317–328 (2001).
 46. W. N. D'Souza, C. F. Chang, A. M. Fischer, M. Li, S. M. Hedrick, The Erk2 MAPK regulates CD8 T cell proliferation and survival. *J. Immunol.* **181**, 7617–7629 (2008).
 47. R. Ley, K. Balmanno, K. Hadfield, C. Weston, S. J. Cook, Activation of the ERK1/2 signaling pathway promotes phosphorylation and proteasome-dependent degradation of the BH3-only protein, Bim. *J. Biol. Chem.* **278**, 18811–18816 (2003).
 48. Q. Xie, J. Liu, Y. Shan, S. Wang, F. Liu, Substrate determinants for unwinding activity of the DEXH/D-box protein RNA helicase A. *Biochemistry* **57**, 6662–6668 (2018).
 49. T. Aktay, I. A. Ilik, D. Maticzka, V. Bhardwaj, C. P. Rodrigues, G. Mittler, T. Manke, R. Backofen, A. Akhtar, DHX9 suppresses RNA processing defects originating from the Alu invasion of the human genome. *Nature* **544**, 115–119 (2017).
 50. A. Cristini, M. Groh, M. S. Kristiansen, N. Gromak, RNA/DNA hybrid interactome identifies DXH9 as a molecular player in transcriptional termination and R-loop-associated DNA damage. *Cell Rep.* **23**, 1891–1905 (2018).
 51. G. B. Robb, T. M. Rana, RNA helicase A interacts with RISC in human cells and functions in RISC loading. *Mol. Cell* **26**, 523–537 (2007).
 52. Q. Fu, Y. A. Yuan, Structural insights into RISC assembly facilitated by dsRNA-binding domains of human RNA helicase A (DHX9). *Nucleic Acids Res.* **41**, 3457–3470 (2013).
 53. A. Jain, A. Bacolla, I. M. del Mundo, J. Zhao, G. Wang, K. M. Vasquez, DHX9 helicase is involved in preventing genomic instability induced by alternatively structured DNA in human cells. *Nucleic Acids Res.* **41**, 10345–10357 (2013).
 54. J. D. Buenrostro, P. G. Giresi, L. C. Zaba, H. Y. Chang, W. J. Greenleaf, Transposition of native chromatin for fast and sensitive epigenomic profiling of open chromatin, DNA-binding proteins and nucleosome position. *Nat. Methods* **10**, 1213–1218 (2013).
 55. B. Langmead, S. L. Salzberg, Fast gapped-read alignment with Bowtie 2. *Nat. Methods* **9**, 357–359 (2012).
 56. Y. Zhang, T. Liu, C. A. Meyer, J. Eeckhoutte, D. S. Johnson, B. E. Bernstein, C. Nusbaum, R. M. Myers, M. Brown, W. Li, X. S. Liu, Model-based analysis of ChIP-Seq (MACS). *Genome Biol.* **9**, R137 (2008).
 57. M. Liao, Y. Liu, J. Yuan, Y. Wen, G. Xu, J. Zhao, L. Cheng, J. Li, X. Wang, F. Wang, L. Liu, I. Amit, S. Zhang, Z. Zhang, Single-cell landscape of bronchoalveolar immune cells in patients with COVID-19. *Nat. Med.* **26**, 842–844 (2020).
 58. T. Stuart, A. Butler, P. Hoffman, C. Hafemeister, E. Papalexi, W. M. Mauck III, Y. Hao, M. Stoeckius, P. Smibert, R. Satija, Comprehensive integration of single-cell data. *Cell* **177**, 1888–1902.e21 (2019).

Acknowledgments: We thank X. Wang, G. Zhang, and B. Lai for flow cytometry analysis and cell sorting. We also thank the Mouse Facility of Xi'an Jiaotong University. **Funding:** B.Z. was, in part, supported by the National Natural Science Foundation of China (grant 81771673), Major International (Regional) Joint Research Project (grant 81820108017), Young Talent Program of Xi'an Jiaotong University (grant YX1J005), and National Young Talent Program. L.Z. was, in part, supported by CAMS Innovation Fund for Medical Sciences (CIFMS 2021-1-I2M-061), the National Natural Science Foundation of China (grant 81971466), and the Non-profit Central Research Institute Fund of Chinese Academy of Medical Sciences (2020-PT310-006). **Author contributions:** B.Z. and L.Z. designed research and interpreted data. A.J., C.S., X.Y., X.W., W.L., H.L., H.Z., R.D., L.L., K.Z., Y.S., and C.Z. performed the experiments and analyzed the data. A.J., C.S., C.Z., and X.Y. analyzed the data. B.Z., A.J., and L.Z. wrote the paper. **Competing interests:** The authors declare that they have no competing interests. **Data and materials availability:** All data needed to evaluate the conclusions in the paper are present in the paper and/or the Supplementary Materials. The sequencing data presented in this paper are available for download on GEO data repository with the following accession numbers: GSE161698, GSE161694, and GSE161697. RNA-seq is available at www.ncbi.nlm.nih.gov/geo/query/acc.cgi?acc=GSE161698, ChIP-seq is available at www.ncbi.nlm.nih.gov/geo/query/acc.cgi?acc=GSE161694, and ATAC-seq is available at www.ncbi.nlm.nih.gov/geo/query/acc.cgi?acc=GSE161697.

Submitted 3 July 2021
 Accepted 14 December 2021
 Published 9 February 2022
 10.1126/sciadv.abk2691